

Utah State University

DigitalCommons@USU

---

All Graduate Theses and Dissertations

Graduate Studies

---

8-2017

## Neutro-Connectedness Theory, Algorithms and Applications

Min Xian

*Utah State University*

Follow this and additional works at: <https://digitalcommons.usu.edu/etd>



Part of the [Computer Sciences Commons](#)

---

### Recommended Citation

Xian, Min, "Neutro-Connectedness Theory, Algorithms and Applications" (2017). *All Graduate Theses and Dissertations*. 6527.

<https://digitalcommons.usu.edu/etd/6527>

This Dissertation is brought to you for free and open access by the Graduate Studies at DigitalCommons@USU. It has been accepted for inclusion in All Graduate Theses and Dissertations by an authorized administrator of DigitalCommons@USU. For more information, please contact [digitalcommons@usu.edu](mailto:digitalcommons@usu.edu).



NEUTRO-CONNECTEDNESS THEORY, ALGORITHMS AND APPLICATIONS

by

Min Xian

A dissertation submitted in partial fulfillment  
of the requirements for the degree

of

DOCTOR OF PHILOSOPHY

in

Computer Science

Approved:

---

Heng-Da Cheng, Ph.D.  
Major Professor

---

Lie Zhu, Ph.D.  
Committee Member

---

Curtis Dyreson, Ph.D.  
Committee Member

---

Haitao Wang, Ph.D.  
Committee Member

---

Kyumin Lee, Ph.D.  
Committee Member

---

Mark R. McLellan, Ph.D.  
Vice President for Research and  
Dean of the School of Graduate Studies

UTAH STATE UNIVERSITY  
Logan, Utah

2017

Copyright © Min Xian 2017

All Rights Reserved

## ABSTRACT

Neutro-Connectedness Theory, Algorithms and Applications

by

Min Xian, Doctor of Philosophy

Utah State University, 2017

Major Professor: Heng-Da Cheng, Ph.D.

Department: Computer Science

Connectedness is an important topological property and has been widely studied in digital topology. However, three main challenges exist in applying connectedness to solve real world problems: (1) the definitions of connectedness based on the classic and fuzzy logic cannot model the “hidden factors” that could influence our decision-making; (2) these definitions are too general to be applied to solve complex problem; and (4) many measurements of connectedness are heavily dependent on the shape (spatial distribution of vertices) of the graph and violate the intuitive idea of connectedness.

This research focused on solving these challenges by redesigning the connectedness theory, developing fast algorithms for connectedness computation, and applying the newly proposed theory and algorithms to solve challenges in real problems.

The newly proposed Neutro-Connectedness (NC) generalizes the conventional definitions of connectedness and can model uncertainty and describe the part and the whole relationship. By applying the dynamic programming strategy, a fast algorithm was proposed to calculate NC for general dataset. It is not just calculating NC map, and the

output NC forest can discover a dataset's topological structure regarding connectedness.

In the first application, interactive image segmentation, two approaches were proposed to solve the two most difficult challenges: user interaction-dependence and intense interaction. The first approach, named NC-Cut, models global topologic property among image regions and reduces the dependence of segmentation performance on the appearance models generated by user interactions. It is less sensitive to the initial region of interest (ROI) than four state-of-the-art ROI-based methods. The second approach, named EISeg, provides user with visual clues to guide the interacting process based on NC. It reduces user interaction greatly by guiding user to where interacting can produce the best segmentation results.

In the second application, NC was utilized to solve the challenge of weak boundary problem in breast ultrasound image segmentation. The approach can model the indeterminacy resulted from weak boundaries better than fuzzy connectedness, and achieved more accurate and robust result on our dataset with 131 breast tumor cases.

(100 pages)

## PUBLIC ABSTRACT

## Neutro-Connectedness Theory, Algorithms and Applications

Min Xian

Connectedness plays an important role in human cognitive and learning activities. Human vision system is very sensitive to the connectedness property of objects and effective in “calculating” the property. The study of connectedness will help us explore the way of human brain extracting the global properties of objects, and enable different avenues to design new artificial intelligent (AI) systems with better performances.

However, connectedness is rarely considered in current AI systems because of the lack of complete theoretic system and efficient computation algorithm. In this work, I focus on building the connectedness theory and algorithms in digital space, and apply them to solve many challenging problems in natural image and low-quality biomedical image segmentation.

The newly proposed Neutro-Connectedness (NC) theory makes it possible to describe the part and the whole relationship and to model the “hidden factors” influencing the decision-making. By applying the dynamic programming strategy, a fast algorithm is proposed to calculate NC for general dataset. It calculates the NC map, and also outputs the NC forest to discover the topological structure of a dataset. The power of NC is demonstrated by applying it to solve two challenging applications: interactive image segmentation (IIS) and breast ultrasound image segmentation (BUSIS).

## ACKNOWLEDGMENTS

I would like to express my sincere gratitude to my advisor, Dr. Heng-Da Cheng, for his strong support for me during my Ph.D. studies. I would never be able to finish this dissertation without his patient guidance. I am very grateful to my committee members, Dr. Lie Zhu, Dr. Curtis Dyreson, Dr. Haitao Wang and Dr. Kyumin Lee for their great comments, advice, and contributions to this research.

I wish to thank my colleagues and friends at Utah State University. Special thanks to my current and previous colleagues, Boyu Zhang, Kaige Zhang, Kuan Huang, Shan Gai, Chenguang Liu, Jianrui Ding, Yingtao Zhang and Rongrong Ni for their help.

I would like to thank my wife, Fei Xu, for her warm encouragement and moral support at all the time. My sincere appreciation goes to my parents and parents-in-law, who helped me taking care of my two little sons. Thanks to my two little sons, Arthur and Cary, they are my endless source of power.

Special thanks to the support of my collaborators from the Second Affiliated Hospital of Harbin Medical University, the Affiliated Hospital of Qingdao University, and the Second Hospital of Hebei Medical University. Thanks to them for helping me collect the breast ultrasound images.

Min Xian

## CONTENTS

|   | Page |
|---|------|
| ABSTRACT .....  | iii  |
| PUBLIC ABSTRACT .....                                     | v    |
| ACKNOWLEDGMENTS .....                                     | vi   |
| LIST OF TABLES .....                                      | ix   |
| LIST OF FIGURES .....                                     | x    |
| CHAPTER   |      |
| 1. INTRODUCTION.....                                      | 1    |
| 1.1 Background .....                                      | 1    |
| 1.2 Related Work .....                                    | 4    |
| 1.2.1 Rosenfeld's Fuzzy Connectedness .....               | 4    |
| 1.2.2 Chen's Fuzzy Subfiber and Fuzzy Connectedness ..... | 6    |
| 1.2.3 Fuzzy Aggregated Connectedness (FACT) .....         | 7    |
| 1.2.4 Connectivity.....                                   | 9    |
| 1.3 Outline.....  | 9    |
| 2. NEUTRO-CONNECTEDNESS THEORY .....                      | 11   |
| 2.1 Basic Idea .....                                      | 11   |
| 2.2 Neutro-Connectedness Theory.....                      | 11   |
| 2.2.1 Neutro-Subset and Its Operations .....              | 12   |
| 2.2.2 NC Definitions and Propositions .....               | 13   |
| 2.3 General Algorithms for NC Computation.....            | 16   |
| 2.4 NC vs. FC.....  | 20   |
| 3. NEUTRO-CONNECTEDNESS CUT .....                         | 21   |
| 3.1 Interactive Image Segmentation (IIS) .....            | 21   |
| 3.2 Neutro-Connectedness Cut Overview .....               | 24   |
| 3.3 NC Computation for Image Regions .....                | 26   |
| 3.4 NC-Cut Formulation .....                              | 26   |
| 3.5 NCF Update .....                                      | 32   |
| 3.6 Optimization .....                                    | 35   |
| 3.7 Dataset, Metrics, and Parameter Settings .....        | 36   |
| 3.8 Experimental Results of Interaction Dependence.....   | 37   |
| 3.9 Overall Performance .....                             | 40   |
| 4. EFFECTIVE INTERACTIVE SEGMENTATION .....               | 43   |



|  |    |
|--|----|
| 4.1 Overview .....   | 43 |
| 4.2 Boundary Connectedness Computation.....                  | 44 |
| 4.3 Protocols for User Interactions .....                    | 44 |
| 4.4 EISeg Formulation and Optimization .....                 | 46 |
| 4.5 Experimental Results .....                               | 49 |
| 5. NC FOR FULLY AUTOMATIC BUS IMAGE SEGMENTATION .....       | 51 |
| 5.1 Background .....   | 51 |
| 5.2 A Short Review of BUS Image Segmentation Approaches..... | 52 |
| 5.3 Overview of the Proposed Approach.....                   | 60 |
| 5.4 Preprocessing .....                                      | 60 |
| 5.5 Adaptive Reference Point Generation .....                | 62 |
| 5.6 Seed Generation .....                                    | 66 |
| 5.7 Adaptive Reference Point Generation .....                | 67 |
| 5.8 Experimental Results .....                               | 70 |
| 5.8.1 Dataset, Parameters, and Metrics .....                 | 70 |
| 5.8.2 Results .....  | 71 |
| 6. CONCLUSION AND FUTURE WORK.....                           | 76 |
| REFERENCES .....   | 78 |
| CURRICULUM VITAE .....                                       | 85 |

## LIST OF TABLES

| Table  | Page |
|--|------|
| 3.1 Average Performance on Dataset DS1.....                    | 41   |
| 3.2 Average Performance on Dataset DS2.....                    | 41   |
| 4.1 Overall Performance on NC-Cut Dataset [16].....            | 50   |
| 5.1 Average Performance of Tumor Segmentation Approaches. .... | 75   |

## LIST OF FIGURES

| Figure  | Page |
|---|------|
| 2.1 A simple example of Neutro-Connectedness Computation. ....                | 19   |
| 3.1 Flowchart of NC-Cut. ....   | 25   |
| 3.2 NC computation of nature images.....                                      | 25   |
| 3.3 Four possible labeling schemes (cuts) for two adjacent nodes in NCF. .... | 29   |
| 3.4 Candidate object and background regions. ....                             | 34   |
| 3.5 Five examples.....  | 38   |
| 3.6 Segmentation performance according to different ROI looseness.....        | 39   |
| 3.7 Failure case.....   | 42   |
| 4.1 Flowchart of EISeg. ....  | 45   |
| 4.2 Example of labeling seed regions. ....                                    | 46   |
| 4.3 Interaction effectiveness.....  | 50   |
| 5.1 Flowchart of the proposed fully automatic BUS segmentation approach.....  | 59   |
| 5.2 RP generation for a synthetic image. ....                                 | 62   |
| 5.3 The seed generation of four BUS images. ....                              | 68   |
| 5.4 Domain reduction functions.....   | 69   |
| 5.5 Calculating connectedness of two BUS images.....                          | 72   |
| 5.6 Deneutrosophication. ....   | 72   |
| 5.7 BUS image segmentation.....   | 74   |

# CHAPTER 1

## INTRODUCTION

### 1.1 Background

Connectedness is an important topological property meaning, in an intuitive sense, “all one piece”. In conventional definition, connectedness describes two states of a mathematical object: if we say an object has the property of connectedness, each component of the object must be connected with all other components; otherwise at least one component is disconnected to other components.

Connectedness is mostly discussed in topology. It is one of the main topological properties utilized to distinguish different topological spaces. In topology, if we say a topological space has the property of connectedness if and only if it cannot be partitioned into two disjoint nonempty open sets, otherwise it does not have the property of connectedness. There are two definitions associated with topological connectedness: path connectedness and local connectedness.

Path connectedness is stronger than the definition of connectedness. For every pair of points in a topological space, it requires a path between any two points in the topological space. For example, subsets of  $R^2$  space are connected if and only if they are path-connected, which means that we can draw a path between any two points in the space. Local connectedness: if a space  $X$  is called locally connected if for each point  $x \in X$  and, for its neighborhood  $N$ , there exists an open set  $U$  that  $x \in U \subset N$ . If  $U$  is path connected,  $X$  can be said to be locally path connected. A locally path connected space is locally connected.

Path connectedness and connectedness describe a space as a whole and are the global properties of a space. Local connectedness and local path connectedness are utilized

to describe the local properties of a space. Generally, global connectedness cannot guarantee local connectedness, and vice-versa. For example, let  $X = (0.1, 0.5) \cup (0.5, 1]$ ;  $X$  does not have the properties of connectedness and path connectedness, but  $X$  is locally connected and locally path connected.

Within the context of graph theory, a graph is called connected (has the property of connectedness) if every two vertices are joined by a path in the graph. The definition is the same with path connectedness in topology. A measure of connectedness, named clustering coefficient is proposed in graph theory. It measures the degree to which nodes in a graph tend to cluster together and has been defined both locally and globally. The global clustering coefficient gives an overall measurement of a graph, while the local version was designed to quantify the embeddedness of single nodes.

The global clustering coefficient is based on the triplets of graph vertices and defined by

$$C^g = \frac{\sum \tau c}{\sum \tau} \quad (1)$$

where  $\sum \tau$  is the total number connected triplets and  $\sum \tau c$  is the number of closed triplets ( $3 \times$  number of triangles); a connected triplet is defined to be a connected subgraph with three vertices and two edges. Opsahl et al. [1] proposed a generalization to weighted networks, in which the global clustering coefficient is defined as the total weights of all closed triplets over the total weights of all connected triplets.

Let  $N_i$  be a set containing all the neighbors a vertex  $v_i$ , and  $k_i$  be the number of vertices of  $N_i$ ; the local clustering coefficient [2] for directed graphs is given as

$$C^l = \frac{\sum e_{N_i}}{k_i(k_i - 1)} \quad (2)$$

where  $\sum e_{N_i}$  is the number of edges between the vertices in  $N_i$ . For undirected graphs, the local clustering coefficient is defined as  $2C^l$ .

The term connectivity has intuitive similarity with connectedness. In graph theory, the connectivity of a graph is the minimum number of vertices that should be removed to create a disconnected graph; for example, if a graph is 4-connected, we must remove four vertices to disconnect it.

Topological properties play an important role in human understanding of the environment due to the high sensitivity of human visual system to global topological properties [3]. As an important topological property, connectedness is utilized as a criterion of unity and can be computed by our visual system effectively [4], which has inspired the solutions of many tasks in image segmentation, object detection, visual saliency estimation, biomedical image analysis, data clustering, topological data analysis, etc.

However, both theoretic and practical challenges exist in applying connectedness to solve real world problems: (1) in topology, the definitions of connectedness are based on classic logic (connected or disconnected); these definitions cannot handle real world problems with uncertainty issue; (2) the connectedness definitions in topology are too general and no guideline exists to discuss how to design quantitative measurement; (3) in graph theory, the global and local clustering coefficients could be applied to measure the degree of connectedness; however, the two measure view a graph or the neighbors of a vertex as a whole, they cannot describe and measure the relationship between the part and the whole; (4) the local and global clustering coefficients are heavily dependent on the

shape (spatial distribution of vertices) of the graph.

To solve these challenges mentioned above, the author conducted research in the following three topics:

- (1) Redesign the theory of connectedness to make it have the ability of modelling uncertainty and describe the part and the whole relationship; both the degree of connectedness and the confidence of the connectedness are introduced in the newly proposed Neutro-Connectedness (NC) theory;
- (2) Design fast algorithm to compute NC; and
- (3) Apply NC to model data topology and solve challenges in real problems such as interactive image segmentation, breast tumor detection, and visual saliency estimation.

## 1.2 Related Work

Connectedness of topological and digital spaces has been widely studied and obtained popularity in digital image processing.

### 1.2.1 Rosenfeld's Fuzzy Connectedness

Fuzzy connectedness (FC) is the first extension of the original definitions of connectedness and redefines connectedness by using the idea of fuzzy set/subset and fuzzy relationship. The first definition of fuzzy connectedness was given in [5] by Rosenfeld in 1979. Rosenfeld [5] generalized the topological concepts such as connectedness and surroundings to fuzzy subsets on 2D space.

Let  $\Sigma_2$  be a two-dimensional array of integer coordinate points,  $S = \{(p, \mu(p)) \in$

$[0, 1]$  be a fuzzy subset of  $\Sigma$  and  $\rho = (p = p_1, p_2, \dots, p_n = q)$  be any path between points  $p$  and  $q$ ; the strength of  $\rho$  [5] is defined by

$$s_r(\rho) = \min_{i=1, \dots, n} \mu(p_i) \quad (3)$$

In Eq. (3),  $s(\rho)$  defines as the weakest membership values of all points along the path  $\rho$ ; and the degree of connectedness (FC) of points  $p$  and  $q$  is given by

$$c_r(p, q) = \max_{\rho \in \mathbb{P}} s(\rho) \quad (4)$$

where  $\mathbb{P}$  is a set consisting of all paths between points  $p$  and  $q$ ; and  $c(p, q)$  uses the strongest path to define the FC between two points. For and subset  $T \subseteq \Sigma_2$ , the FC of  $T$  is defined by

$$c_r(T) = \min_{p, q \in T} c_r(p, q) \quad (5)$$

Rosenfeld [5] also discussed three important properties of FC:

$$(1) c_r(p, p) = \mu(p), c_r(p, q) = c_r(q, p)$$

$$(2) c_r(p, q) \leq \min(\mu(p), \mu(q))$$

$$(3) c_r(T) \leq \min_{p \in T} \mu(p)$$

The above three properties are quite useful in designing algorithms to calculate FC and Eqs. (3), (4) and (5) offer the base for almost all variants of FC definitions. Several drawbacks exist in Rosenfeld's FC:

- (1) The FC is build based on the fuzzy set concept, for a specific task, researcher need to have domain related knowledge to define the membership function; this is possible in applications in which we could know what objects we are dealing with; however, in many applications such as interactive image segmentation,



we have no clue about what user could like to segment out from an image; therefore, it is impossible to pre-design any membership function for the task.

- (2) In [5], two points  $p$  and  $q$  are said to be connected if  $c(p, q) = \min(\mu(p), \mu(q))$ . This definition implies that all membership values along the strongest path should be greater than or equal to  $\min(\mu(p), \mu(q))$ . This definition is too strong and cannot handle noisy data well.
- (3) No algorithm was proposed to calculate the FC.

### 1.2.2 Chen's Fuzzy subfiber and Fuzzy Connectedness

Chen et al. [6] proposed the fuzzy subfiber and extended the FC definitions to deal with tasks of multi-dimensional space. Let  $\Sigma_N$  be a  $N$ -dimensional digital space; an  $(N, n)$  subfiber is defined by

$$S_c = \{(p, f(p)) \mid f: \Sigma_N \rightarrow [0,1]^n, p \in \Sigma_N\} \quad (6)$$

In Eq. (6),  $f$  defines a  $N$ -to- $n$  mapping; when  $N = 2$ , and  $n = 1$ ,  $S_c$  is the Rosenfeld's 2D fuzzy subset.

The definition of FC in [6] follows the basic idea of Rosenfeld's FC ( $c_r$ ): the strength of a path is determined by the weakest point along the path and the degree of connectedness of any two points is determined by the strongest path between the two points. However, Chen et al. [6] did not define FC by using the membership values ( $f$ ), but by using a newly proposed function named adjacency function. The function defines the degree of adjacency between two points:

$$A(p, q) = \begin{cases} E(f(p), f(q)), & p \text{ and } q \text{ are adjacent} \\ 0, & \text{otherwise} \end{cases} \quad (7)$$

In Eq. (7),  $E$  measures the similarity of two vectors and outputs a scalar in  $[0, 1]$ ;  $E$  should satisfy  $E(p, p) = 1$  and  $E(p, q) = E(q, p)$ . Two examples  $E$  were given in [6]:

$$E_1(f(p), f(q)) = \begin{cases} 1 - \frac{\|f(p) - f(q)\|}{\|f(p)\| + \|f(q)\|}, & \|f(p)\| + \|f(q)\| \neq 0 \\ 1, & \text{otherwise} \end{cases} \quad (8)$$

$$E_2(f(p), f(q)) = 1 - \frac{\|f(p) - f(q)\|}{\max_{p, q \in \Sigma_N} \{\|f(p) - f(q)\|\}} \quad (9)$$

The strength of a path  $\rho = (p = p_1, p_2, \dots, p_n = q)$  in [6] is defined by

$$s_c(\rho) = \min_{i=1, \dots, n-1} A(p_i, p_{i+1}) \quad (10)$$

and the degree of connectedness of any two points  $p$  and  $q$  is given as

$$c_c(p, q) = \max_{\rho \in \mathbb{P}} s_c(\rho) \quad (11)$$

where  $\mathbb{P}$  is a set consisting of all paths between points  $p$  and  $q$ .

The new definition in [6] extends the ability of FC to handle high-dimensional data; and because  $f(p)$  could be feature vector of point  $p$ , which makes  $c_c$  and  $s_c$  less dependent on the domain-related knowledge. The drawback of [6] is that no effective algorithm was proposed to calculate  $c_c$ .

Udupa et al. [7, 8] designed algorithms of FC to solve tasks such as object extraction, image segmentation and classification.

### 1.2.3 Fuzzy Aggregated Connectedness (FACT)

He et al. [9] stated that always choosing the best (strongest) path to calculate the FC makes FC sensitive to noise; and the crisp decision of preserving or discarding a path violated the concept of fuzzy sets; therefore, they proposed the fuzzy aggregated connectedness (FACT) for image segmentation by using a group of paths to calculate FC.

Let  $f(p)$  be the feature vector of point  $p$  and  $A_h \in [0, 1]$  be the feature similarity of two adjacent points, He et al. defined the strength of a path  $\rho = (p = p_1, p_2, \dots, p_n = q)$  by

$$s_h(\rho) = \prod_{i=1}^{n-1} A_h(p_i, p_{i+1}) \quad (12)$$

$s_h(\rho)$  is calculated by multiplying all  $A_h$  values along the path  $\rho$ ; only when all the data points along the path located closely along the path in the feature space, the strength of path  $\rho$  could be large. The FACT was defined by

$$c_h(p, q) = \left( \sum_{\rho \in \mathbb{P}_{cd}} \frac{s_h(\rho)}{\text{card}(\mathbb{P}_{cd})} \right)^{1/l} \quad (13)$$

where  $\mathbb{P}_{cd}$  is a set containing all the paths between points  $p$  and  $q$ ,  $\text{card}(\mathbb{P}_{cd})$  is the cardinal number of set  $\mathbb{P}_{cd}$ , and  $l = |p_x - q_x| + |p_y - q_y|$  is the length of the paths in  $\mathbb{P}_{cd}$ ;  $c_h(p, q)$  only considers the paths with length  $l$  in a local region bounded by  $p$  and  $q$ .

Three problems exist in the definition of FACT: (1) the strength of a path  $s_h(\rho)$  is determined by the smallest value in  $A_h$  ( $A_h \in [0, 1]$  and  $s_h(\rho) \leq \min\{A_h(p_i, p_{i+1})\}$ ); and the chain-multiplication makes the calculation of FACT computational-intensive; (2)  $s_h(\rho)$  is sensitive the length of a path; if  $A_h \in (0, 1)$ , the strength of longer path is always smaller than the strength of a shorter path. This idea is quite different to the original definitions in [5] and [6]; and (3)  $c_h$  considers all the paths in a local region, which has no problem for objects or image regions with convex shapes; however, it cannot deal with regions with nonconvex shapes.

He et al. [9] applied FACT for image segmentation. However, no detail and analysis

of the algorithm performance were reported; and only two images were applied for evaluation.

#### 1.2.4 Connectivity

Connectedness has been widely employed in image segmentation [6-8, 10, 11]. In classic logic, the connectedness between any pair of elements is defined as whether there exists a path between them (path connectedness). In fuzzy logic, FC is defined as the degree of connectedness between two elements. In [10], an interactive segmentation method based on FC [6, 7] and Graph cuts [12] was proposed. In digital topology, connectivity defines the condition of adjacency between points, which is similar to the connectedness defined on classic logic. Connectivity [13, 14] is usually employed to solve the “shrinking bias” problem in Graph cuts. The connectivity constraint is usually formulated using a shortest geodesic path tree computed by Dijkstra’s algorithm, and user only utilize a point or a region as the root node. However, the method cannot achieve good performance for segmenting objects with complicated appearance. The geodesic distance accumulates the distances between adjacent nodes along the shortest path [13, 14]. On a path, the farther a node from the source, the larger distance the node has. The connectedness is a global topology property independent of the length of the path. Therefore, the geodesic distance is not suitable for defining connectedness.

#### 1.3 Outline

In this dissertation, I will present my work in Neutro-Connectedness (NC) theory, algorithms, and how to apply NC to solve many challenging problems in interactive image segmentation and breast tumor segmentation.

In Chapter 2, the newly proposed Neutro-Connectedness (NC) theory and its properties are presented and discussed; the new definitions of NC introduce a new domain, named the confidence of connectedness, to model the indeterminacy of connectedness. With the additional domain, NC is capable of dealing with more complex problems, e.g., low quality image segmentation, and noisy data analysis. A general fast algorithm for NC computation is also given in this section; the algorithm can output NC map (matrix) and the structure of connectedness (NC forest) at the same time. In Chapters 3 and 4, two algorithms, NC-Cut and EISeg, are presented. The two algorithms are designed to improve the robustness of interactive image segmentation (IIS) to user interactions by applying NC. In NC-Cut, we generalize the Neutro-Connectedness (NC) to be independent of top-down priors of objects and to model image topology with indeterminacy measurement on image regions and put forward a hybrid interactive segmentation method which utilizes both pixel-wise appearance information and region-based NC properties. The effective interactive segmentation (EISeg) method provides user with objective visual clues for guiding interactions by using NC map and NC forest; The experiments demonstrate that the proposed EISeg method guides interaction effectively, and achieves better results with much less user interaction than state-of-the-art approaches. In Chapter 5, a new breast tumor detection algorithm is proposed by modeling tumor structure using NC. Much progress has been made on applying fuzzy connectedness to segment objects from low quality images. However, the fuzzy connectedness method still has difficult in segmenting objects with weak boundaries. In the chapter, we apply NC to model the inherent uncertainty and indeterminacy of the spatial topological properties of the image. In Chapter 6, the conclusion and my future work are discussed.

## CHAPTER 2

### NEUTRO-CONNECTEDNESS THEORY AND ALGORITHM

#### 2.1 Basic Idea

As discussed in section 1.2, the connectedness theory is built on the concept of fuzzy set/subset and fuzzy connectedness is the most fundamental and popular way of defining the degree of connectedness in digital space. However, the classical “Reviewers’ Problem” [11] shows that some tasks cannot be solved by fuzzy set-based approaches: two reviewers (A and B) rank a paper with memberships  $\mu_A$  and  $\mu_B$ . Assume that  $\mu_A = \mu_B = 0.8$ , and they have different background qualifications. Although they give the same membership, the two membership values will have different effects on the paper decision. This problem reveals that, besides the membership, some factors may also influence the final decision, e.g., a reviewer’s academic background and paper reviewing history.

The message we can take from the “Reviewers’ Problem” is that some hidden factors behind the membership functions could play an important role in decision making; and in defining the degree of connectedness, we should consider the “hidden factors”, e.g., signal noise ratio (SNR), local homogeneity, and outliers. Therefore, we generalize the theory of FC by proposing the Neutro-Connectedness theory which has one additional domain, confidence of connectedness, utilized to model the “hidden factors”.

#### 2.2 Neutro-Connectedness Theory

We propose Neutro-connectedness (NC) first in [16], and applied to solve the weak boundary problem in breast ultrasound (BUS) image segmentation. The NC in [16] is a top-down method based on the priori information of the object and background. In this

section, we will generalize the NC definition in [16] to make it independent of the top-down priors of objects.

In NC, the fuzzy set/subset concept is extended to contain two domains. As discussed in section 1.2, Rosenfeld [5] proposed the concept of 2D fuzzy subset and related methods on grayscale image. L. Chen et al. [6] extended the 2D fuzzy subset to handle the spatial uncertainty in multidimensional data by introducing the concept of fuzzy subfiber. Based on the membership function, the above two methods could model the imprecision of the data; however, both of the approaches did not take the “hidden factors” into consideration.

### 2.2.1 Neutro-Subset and Its Operations

Definition 1: Let  $U$  be a universe of discourse, a Neutro-Subset is defined by

$$S_x = \left\{ \left( p, (T(p), C(p)) \right) \mid p \in U \right\} \quad (14)$$

where  $p$  is an arbitrary  $N$ -dimensional data point in  $U$ , and  $T$  and  $C$  defines the degree of connectedness and confidence of connectedness, respectively.  $T$  and  $C$  could be  $n$ -dimensional vectors  $([0, 1]^n)$ , when  $C(p) = [0]^n, \forall p \in U$ , the Neutro-Subset becomes the fuzzy subfiber; and if  $N = 2, n = 1$  and  $C(p) = [0]^n, \forall p \in U$ , it becomes the fuzzy subset.

In Eq. (14), every  $T$  value in the Neutro-Subset is associated with a  $C$  value to show the confidence of the  $T$  value, and the additional  $C$  values gives the ability of Neutro-Subset to carry more information. Fuzzy subset and fuzzy subfiber become special cases of the Neutro-Subset.

Define two Neutro-Subsets  $A = \left\{ \left( p, (T_A(p), C_A(p)) \right) \mid p \in U \right\}$  and  $B =$

$\{(p, (T_B(p), C_B(p))) \mid p \in U\}$  on  $U$ . Basic set operations of union, intersection and complement are defined as follows.

$$\text{Union } A \cup B = \{(p, TC_{\succ}(T_A(p), C_A(p), T_B(p), C_B(p))) \mid p \in U\} \quad (15)$$

$$\text{Intersection } A \cap B = \{(p, TC_{\preccurlyeq}(T_A(p), C_A(p), T_B(p), C_B(p))) \mid p \in U\} \quad (16)$$

$$\text{Complement } \bar{A} = \{(p, (1 - T_A(p), C_A(p))) \mid p \in U\} \quad (17)$$

In Eq. (15), operators  $\succ$  and  $\preccurlyeq$  define two partial relations;  $TC_{\succ}(a, b, c, d)$  outputs  $(a, b)$  if and only if  $a > c$  or  $(a = c \text{ and } b \geq d)$ ; otherwise, outputs  $(c, d)$ .  $TC_{\preccurlyeq}(a, b, c, d)$  outputs  $(a, b)$  if and only if  $a < c$  or  $(a = c \text{ and } b \leq d)$ ; otherwise, outputs  $(c, d)$ .

Because fuzzy set is a special case of Neutro-Subset holds all the properties of fuzzy set such as commutativity, associativity, distributivity, Idempotency, etc.

### 2.2.2 NC Definitions and Propositions

Definition 2: Let  $\mathcal{U}$  be the set of all data points, and  $Z_i$  be the  $i$ th path between two points in  $\mathcal{U}$ . The strength of the path  $Z_i$  is defined by

$$NC_{path}(Z_i) = (\Pi^T(Z_i), \Pi^C(Z_i)) \quad (18)$$

$$Z_i = (z_1, z_2, \dots, z_L), z_k \in \mathcal{U}, k = 1, 2, \dots, L$$

where  $L$  is the number of points on  $Z_i$ , and  $z_k$  denotes the  $k$ th point,  $\Pi^T(Z_i)$  and  $\Pi^C(Z_i)$  represent the degree and confidence of the connectedness of path  $Z_i$ , respectively. They are defined as follows.

$$\Pi^T(Z_i) = \min\{\mu_T(z_j, z_k) \mid z_k \in \mathbb{N}(z_j), z_j, z_k \in Z_i\} \quad (19)$$

$$\Pi^C(Z_i) = \min\{\mu_C(z_j, z_k) \mid z_k \in \mathbb{N}(z_j), z_j, z_k \in Z_i\} \quad (20)$$

In Eqs. (19) and (20), we use  $\mathbb{N}(z_j)$  to represent the set of all neighbors of point  $z_j$ ,



$\mu_T$  to represent the strength of connectedness between two adjacent points, and  $\mu_C$  to represent the confidence of the connectedness;  $\mu_T$  and  $\mu_C$  must satisfy

$$\begin{aligned}\mu_T(p, p) &= \mu_T(q, q) = 1 \\ \mu_T(p, q) &= \mu_T(q, p) \text{ and } \mu_C(p, q) = \mu_C(q, p)\end{aligned}\quad (21)$$

An example of  $\mu_T$  and  $\mu_C$  could be defined as follows.

$$\mu_T(p, q) = e^{-\frac{\|m(p)-m(q)\|^2}{2\delta_t^2}} \quad (22)$$

$$\mu_C(p, q) = \min\{h(p), h(q)\} \quad (23)$$

In Eqs. (22) and (23)  $m(p)$  and  $m(q)$  are feature vectors of  $p$  and  $q$ , respectively;  $h(\cdot)$  is the degree of confidence of a data point by calculating its local properties. Eq. (22) penalizes the feature discontinuity between  $p$  and  $q$ : if  $|m(p) - m(q)| < \delta_t$ , Eq. (22) penalizes more; otherwise less.  $h$  could be defined as the degree of homogeneity of the a local region.

Definition 3: Let  $\mathbb{Z}$  be the set of all the paths between  $p$  and  $q$  in set  $\mathcal{U}$ . The *Neutro-Connectedness* between  $p$  and  $q$ ,  $NC(p, q)$ , is defined as.

$$\begin{aligned}NC(p, q) &= \left( (T, C) = NC_{path}(Z_d) \right), Z_d \in \mathbb{Z}, \\ \forall Z_i \in \mathbb{Z}, \langle \Pi^T(Z_i), \Pi^C(Z_i) \rangle &\preceq \langle \Pi^T(Z_d), \Pi^C(Z_d) \rangle\end{aligned}\quad (24)$$

In Eq. (24),  $Z_d$  is the path with the strongest connectedness between  $p$  and  $q$  in set  $\mathbb{Z}$ ;  $T$  and  $C$  are the corresponding degrees and confidence of connectedness between  $p$  and  $q$ , respectively; the operator  $\preceq$  denotes a lexicographical order relation. All the four operators  $\preceq, <, \succcurlyeq$  and  $>$  used in the dissertation are defined by

$$\langle a_1, b_1 \rangle \preceq \langle a_2, b_2 \rangle \Leftrightarrow a_1 < a_2 \text{ or } (a_1 = a_2 \text{ and } b_1 \leq b_2)$$

$$\langle a_1, b_1 \rangle < \langle a_2, b_2 \rangle \Leftrightarrow a_1 < a_2 \text{ or } (a_1 = a_2 \text{ and } b_1 < b_2)$$

$$\langle a_1, b_1 \rangle \succcurlyeq \langle a_2, b_2 \rangle \Leftrightarrow a_1 > a_2 \text{ or } (a_1 = a_2 \text{ and } b_1 \geq b_2)$$

$$\langle a_1, b_1 \rangle \succ \langle a_2, b_2 \rangle \Leftrightarrow a_1 > a_2 \text{ or } (a_1 = a_2 \text{ and } b_1 > b_2) \quad (25)$$

Proposition 1:  $\forall p, q \in U$ , and let  $\mu_T$  and  $\mu_C$  be defined as Eqs. (22) and (23), respectively, we have  $NC(p, p) = (1, h(p))$   $NC(q, q) = (1, h(q))$  and  $NC(p, q) = NC(q, p)$ .

*Proof* According to constraints of Eqs. (22) and (23), we have  $\mu_T(p, p) = \mu_T(q, q) = 1$  and  $\mu_C(p, p) = h(p)$  and  $\mu_C(q, q) = h(q)$ . Let  $\rho = (p)$  be a path with only a single point, the strength of the path  $NC_{path}(\rho)$  is  $(1, h(p))$ . For any path  $\rho' = (p = p_1, p_2, \dots, p_n = p)$  and  $n > 1$ , we have that  $\Pi^T(\rho') \leq 1$  and  $\Pi^C(\rho') = \min_i \{h(p_i)\} \leq h(p)$ . Then we have  $NC_{path}(\rho) = (1, h(p)) \succcurlyeq (\Pi^T(\rho'), \Pi^C(\rho')) = NC_{path}(\rho')$  and so that  $NC(p, p) = (1, h(p))$ . We can also prove that  $NC(q, q) = (1, h(q))$  in the same way.

Let  $\rho = (p = p_1, p_2, \dots, p_n = q)$  be the strongest path from  $p$  to  $q$ , and we have that  $NC(p, q) = NC_{path}(\rho)$ . For the inverse path  $\rho'$  of  $\rho$  from  $q$  to  $p$ ,  $NC_{path}(\rho') = NC_{path}(\rho)$  because of Eqs. (19-21). Now we assume that a path  $\rho'' \neq \rho'$  exists from  $q$  to  $p$  and  $NC(q, p) = NC_{path}(\rho'')$ . Then we have that  $NC_{path}(\rho'') \succcurlyeq NC_{path}(\rho') = NC_{path}(\rho)$ , which contradicts with the assumption that  $\rho$  be the strongest path from  $p$  to  $q$ .

Proposition 2:  $\forall p, q, r \in U$ ,  $NC(p, q) \succ (0, 0)$  and  $NC(q, r) \succ (0, 0)$ , we have that  $NC(p, r) \succ 0$ .

*Proof* Let  $\rho_{pq}$  be the strongest path from  $p$  to  $q$  and  $\rho_{qr}$  be the strongest path between  $q$  and  $r$ , we have that  $NC(p, q) = NC_{path}(\rho_{pq}) \succ (0, 0)$  and  $NC(q, r) = NC_{path}(\rho_{qr}) \succ (0, 0)$ . We link the two paths  $\rho_{pq}$  and  $\rho_{qr}$  and create a path  $\rho_{pr} = (\rho_{pq}, \rho_{qr})$ , then we have that  $NC_{path}(\rho_{pr}) = \min(NC_{path}(\rho_{pq}), NC_{path}(\rho_{qr})) \succ (0, 0)$

and  $NC(p, r) \geq NC_{path}(\rho_{pr}) > (0, 0)$ .

Proposition 3:  $\forall p, q \in U$ , if  $NC(p, q) = (T, C)$ , we have  $NC(p, q) \leq NC(p, p)$ ,  $NC(p, q) \leq NC(q, q)$ .

*Proof* As proved in Proposition 1, we have that  $NC(p, p) = (1, h(p))$  and ,  $NC(q, q) = (1, h(q))$ . Let  $\rho = (p = p_1, p_2, \dots, p_n = q)$  be the strongest path from  $p$  to  $q$ , we have that  $NC(p, q) = (\Pi^T(\rho), \Pi^C(\rho))$ . Because  $\Pi^T(\rho) \leq 1$  and  $\Pi^C(\rho) = \min_i \{h(p_i)\} \leq h(p)$ , so we have  $NC(p, q) \leq NC(p, p)$ . Similarly, we can prove that  $NC(p, q) \leq NC(q, q)$ .

Proposition 4: Let  $\rho = (p = p_1, p_2, \dots, p_n = q)$  be a path from point  $p$  to  $q$  such that  $NC(p, q) = NC_{path}(\rho)$ ; and for any  $i$  and  $j$  such that  $1 \leq i \leq j \leq n$ , let  $\rho_{ij} = (p_i, p_{i+1}, \dots, p_j)$  be any subpath of  $\rho$ . Then  $NC(p_i, p_j) = NC_{path}(\rho_{ij})$ .

*Proof* Because that  $NC(p, q) = NC_{path}(\rho)$ ,  $\rho$  is the strongest path from  $i$  to  $j$ . We can divide  $\rho$  into three parts:  $\rho_{1i}$ ,  $\rho_{ij}$  and  $\rho_{jn}$ , then we have that  $NC_{path}(\rho) = \min\{NC_{path}(\rho_{1i}), NC_{path}(\rho_{ij}), NC_{path}(\rho_{jn})\}$ . Now we assume that a path  $\rho'_{ij} \neq \rho_{ij}$  exists from  $i$  to  $j$  with  $NC(p_i, p_j) = NC_{path}(\rho'_{ij})$ . Then we have  $NC_{path}(\rho'_{ij}) \geq NC_{path}(\rho_{ij})$  and a new path  $(\rho_{1i}, \rho'_{ij}, \rho_{jn})$  whose strength  $\min\{NC_{path}(\rho_{1i}), NC_{path}(\rho'_{ij}), NC_{path}(\rho_{jn})\} \geq NC_{path}(\rho)$ , which contradicts the assumption that  $\rho$  is the strongest path from  $i$  to  $j$ .

### 2.3 General Algorithms for NC Computation

We have proposed the NC computation algorithm for image regions in our previous work [16]. In this section, we extend the original algorithm and propose NC computation

algorithms for general dataset analysis. According to Proposition 4, the NC computation problem exhibits optimal substructure and overlap subproblems, so we could apply the dynamic programming strategy to design the NC computation algorithm. We propose a NC computation algorithm (Algorithm 2.1) which outputs NC quite fast; moreover, Algorithm 2.1 generates the NC forest to explore the topological structure of NC.

---

**Algorithm 2.1: Neutro-Connectedness Computation**

---

Inputs: data point  $x$ ,  $AT = [\mu_T(p, q)]_{N \times N}$  and  $AC = [\mu_C(p, q)]_{N \times N}$

Outputs:  $\{(T_r, C_r)\}_{r=1}^N$ ,  $NCF = \{(pre_r, rt_r)\}_{r=1}^N$

- 1: Initialization:  $(T_r, C_r) = (0, 0), r = 1, 2, \dots, N, (T_x, C_x) = (1, 1)$   
 $pre_x = x, rt_x = x$   
Put  $x$  into a queue  $Q$
  - 2: Extract the point  $p$  with the strongest connectedness to  $x$  on  $Q$  according to  $\succcurlyeq$
  - 3: For each point  $q$  adjacent to  $p$   
if  $\langle T_q, C_q \rangle < \langle \min(T_p, AT(p, q)), \min(C_p, AC(p, q)) \rangle$  then  
 $T_q = \min(T_p, AT(p, q))$  and  $C_q = \min(C_p, AC(p, q))$   
 $pre_q = p$ , and  $rt_q = rt_p$   
Insert  $q$  to  $Q$
  - 4: Repeat steps 2 and 3 until  $Q$  is empty.
- 

As shown in Definitions 2 and 3, the NC value between two data points is defined as a two-tuple  $(T, C)$ . Algorithm 2.1 computes the NC values between every data point and the target point  $x$ ,  $AT$  and  $AC$  are two sparse matrices;  $AT$  saves the similarity between every pair of adjacent points calculated by using Eq. (22);  $AC$  saves the confidence of connectedness (Eq. (23)) of every pair of adjacent points;  $(T_r, C_r)$  is the NC between the  $r$ th data point and data point  $x$ ; and  $pre_r$  and  $rt_r$  denote the parent and root node of node  $r$ , respectively.

There are three main steps in Algorithm 2.1. In the initialization step (step 1), we set  $NC$  of the target point  $x$  to  $(1, 1)$  and its parent node (and root node) is itself; and set the  $NC$  values of all other points to  $(0, 0)$ ; and we create a priority queue  $Q$  to save data points which will be calculated in the next steps;  $Q$  is initialized by using the target point  $x$  and will be updated in steps 2 and 3. Note that  $x$  could be single point or a set of data points

In step 2, every time the point  $p$  with the strongest connectedness to point  $x$  is extracted from  $Q$  based on the  $\succcurlyeq$  operator defined in Eq. (25). Because  $Q$  is designed as a priority queue, so time complexity of the extraction is only  $O(1)$ . In step 3, the  $NC$  values, parent nodes and root nodes of point  $p$ 's neighbors are updated; and the newly updated point is added into the  $Q$ . Algorithm 2.1 repeats steps 2 and 3 until  $Q$  is empty.

The time and space complexities: the time complexity of Algorithm 2.1 depends on how to implement queue  $Q$ . In the first case, if we maintain  $Q$  as an array, both the extraction operation in step 2 and the insertion operation in step 3 take  $O(N)$  time, and the total time of Algorithm 2.1 is  $O(N^2)$ .  $Q$  can be implemented by using max-priority queue, then the insertion operation takes  $O(\log N)$ , then the total time is  $O(N \log N)$ . Since  $AT$  and  $AC$  are both sparse matrices, the space complexity of Algorithm 2.1 is  $O(N)$ . Algorithm 2.1 is a modified version of Dijkstra's method and the best time complexity can be linear [40]. The image foresting transform (IFT) [28] generates spanning forest for image, which is similar to NCF generation process in Algorithm 2.1, and a superpixel implementation of the IFT can be found in [40]; nevertheless, there are two main differences between NCF and IFT: first, the fundamental concept for constructing NCF is taking both the degree and confi-

dence of connectedness into consideration, while IFT constructs spanning forests by selecting the path with the minimum path cost. Second, in the case of ties (two paths with same  $T$  value), IFT follows the last-in-first-out (LIFO) queue policy to break ties; Algorithm 2.1 introduces the lexicographical order relation of  $(T, C)$  to determine the best path.

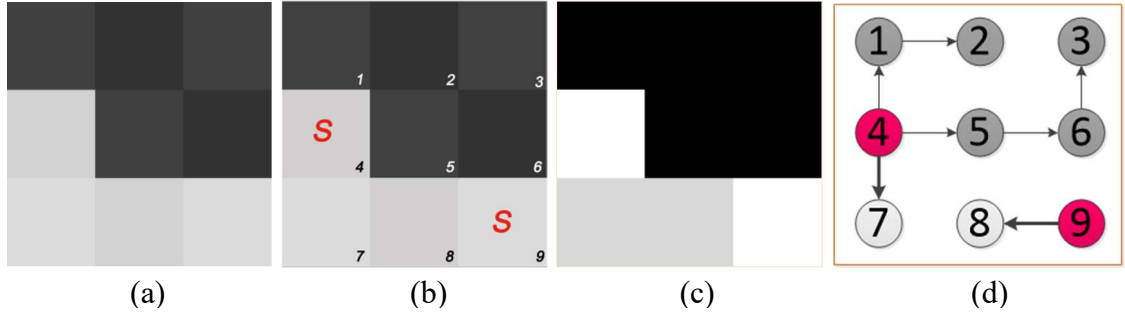


Fig. 2.1. A simple example of Neutro-Connectedness Computation. (a) Nine regions; (b) the region numbers (lower right corner) and seed regions indicated by red ‘S’; (c) the degree of connectedness for each region; (d) NC forest (NCF).

Fig. 2.1 shows an example of NC computation of a synthetic image with nine regions falling into two categories: dark regions (1, 2, 3, 5, and 6) and light regions (4, 7, 8, and 9). Note that region 8 is an inhomogeneous region with Gaussian noise. The fourth and eighth regions are the seed regions ( $x = \{4, 8\}$ ). Fig. 2.1(c) shows the forest (FC-based) and the degree of connectedness ( $T$ ) between each region and the seed regions without considering the confidence of connectedness ( $C$ ), which is the same with the results of FC algorithm; all the light regions have high  $T$  values, and all the dark regions have low  $T$  values; regions 7 and 9 are both connected to seed region 8, and have the same degree of connectedness. Fig. 2.1(d) shows results of the proposed NC; the NCF in Fig. 2.1(d) is different from the forest in Fig. 2.1(c); even though regions 7 and 9 have same  $T$  values

(0.85) to the seed regions, the degree of indeterminacy of region 9 (0.1) is higher than that of region 7 (0) due to the noise.

## 2.4 NC vs. FC

We design Algorithm 2.1 using the dynamic programming strategy. There are three main differences between the proposed NC algorithm and the FC algorithm: first, the proposed algorithm generates NCF, which uncovers the topological structure of NC maps by using trees; second, the proposed algorithm calculates the degrees of connectedness and the confidence of connectedness simultaneously; third, the FC method was designed for image processing; while the proposed method is designed for calculating connectedness for general dataset.

## CHAPTER 3

### NEUTRO-CONNECTEDNESS CUT

In this chapter, NC is applied to achieve robust interactive image segmentation by solving the major challenges of high interaction sensitivity. The main results have been published in [16].

#### 3.1 Interactive Image Segmentation (IIS)

IIS is an interesting and challenging task in image processing. In this task, user extracts objects from image by incorporating interactions such as marking seeds, setting region of interest, etc. The advantage of IIS is that satisfactory segmentation results can always be achieved because it can incorporate priori information (appearance, shape, topology, context, etc.) and correct errors by interactions. However, intense and precise user interactions are needed to segment complicated objects using seed-based approaches, which lead to low usability; although ROI-based methods need much less user interaction, their performances are sensitive to the initial ROI [32].

Many inspiring interactive segmentation methods have been proposed in the last two decades, and in terms of the ways of user interaction, these approaches can be classified into two categories: seed-based [12 - 14, 17 - 25] and region of interest (ROI)-based [26 - 31] approaches.

Live wire [19] and intelligent scissors [20] are two boundary seed-based approaches, and user specify seeds on object boundary to extract objects from image. [19, 20] obtain the final object boundary by computing the shortest path among the seeds. The



two approaches are intuitive, but suffer two main drawbacks: (1) they require user to specify as much seeds as possible, and insufficient seeds will result in low segmentation performance; (2) the seeds need to be accurately placed on real object boundary, which is impossible in many applications such as low-quality image segmentation, mobile device-based segmentation, large number of objects segmentation, etc.

Graph cuts [12] is one of the most popular region seed-based approaches, and both appearances models and boundary constraints are formulized in a combinational optimization framework. The object and background seeds will be utilized to estimate the object and background appearances, respectively. Lots of seeds must be marked in Graph cuts to obtain accurate result; especially, when image has complicated structures, user need to set as many seeds as possible to cover different structures. In [21], the IIS was formulated as a spline regression problem. The parameters in the spline function were estimated by using the user specified object and background pixels, and the labels of all other pixels were determined by the signs of spline function values. However, same with Graph cuts, user must specify quite many seeds to obtain controllable and desired accuracy. Spina et al. [22] proposed a hybrid IIS approach, Live markers, by combining the boundary seed-based methods (Live-wire-on-the-fly [23], Riverbed [24]) and region seed-based methods (Image Foresting Transform (IFT) [25], Graph cuts [12]). Although the method needs less user interaction than traditional boundary seed-based methods, it still requires user to specify seeds on object boundary accurately.

Grabcut [26] is one of the best-known ROI-based IIS methods. User draws ROI (rectangle and polygon) to specify the initial object and background regions. There is only one requirement of the interaction: the ROI should fully contain the object. The regions in

the ROI and outside the ROI are utilized for learning the object and background appearance models, respectively. Grabcut needs much less user interaction and can achieve better segmentation results than graph cuts. However, its performance is quite sensitive to ROI. Han et al. [29] extended the color feature-based GMMs in Grabcut by constructing pixels' features based on color and multiscale nonlinear structure tensor [33]. The method can achieve better results than Grabcut for segmenting images with complex texture, but it still needs tight ROIs to obtain accurate results. PinPoint [27] defined the tightness by employing a user-specified bounding box. The method assumes that the user always specifies tight ROIs; and it cannot obtain high segmentation accuracy if a loose ROI is given.

MILCut [30] formulated IIS as a multiple instance learning (MIL) problem. It generates negative and positive bags from the pixels outside a bounding box and the pixels of sweeping lines within the bounding box, respectively. The segmentation result of MILCut is very sensitive to the size of the initial bounding box. Tang et al. [28] proposed One-cut to incorporate the measurement of  $L_1$  distance between object and background appearance models into the Graph cuts energy function. A graph construction method for high order potentials was also given in their work [28]. One-Cut needs less user interaction than Graph cuts. In [31], Tang et al. proposed a parametric Pseudo-Bound Cuts (pPBC) method for optimizing interactive segmentation with high-order and non-submodular energies. The experiments in section IV demonstrate that pPBC achieves better results than other ROI-based methods (Grabcut, MILCut and One-Cut); however, its performance is still sensitive to the initial ROI.

As mentioned above, there are three main challenges in IIS: (1) intense user interactions are required to segment complicated objects using region seed-based approaches

and precise interactions are needed in boundary seed-based methods, which lead to low usability of these methods; (2) ROI-based methods need much less user interaction, but their performances are sensitive to users' inputs; and (3) in both seed-based and ROI-based approaches, the user interactions have a great arbitrariness which could produce unpredictable results; most methods focus on improving segmentation performance by integrating higher level information; and to the best of our knowledge, no work has been done to provide user with useful information about how to interact can achieve good performance.

In this chapter, we discuss the details and experimental results of Neutro-Connectedness Cut (NC-Cut) algorithm in section 3.2.

NC-Cut is a novel hybrid interactive image segmentation approach, which formulates segmentation based on both pixel-wise appearance models and NC properties. NC models global topologic property among image regions and can reduce the dependence of segmentation performance on the appearance models generated by user interactions. The user interaction is to specify a polygon containing the object, and the image regions outside the polygon are viewed as the background seeds. The NC computation algorithm is utilized to calculate the NC values between each region in the polygon and background seeds, and generates a NC forest rooted from the background seed set. The constructed graph based on NC forest imposes NC as a global constraint to the segmentation.

### 3.2 Neutro-Connectedness Cut Overview

As discussed above, the ROI-based IIS approaches need less user interactions than the seed-based approaches. However, high sensitivity to user interaction is their major problem, and is caused by using user interaction to learn the initial object and background

appearance models. When the user specifies a loose ROI (large portion of background regions in the ROI), the object appearance model will be initialized poorly and result in poor segmentation performance. Our basic idea to solve this problem is to make our segmentation model less sensitive to image appearance models by incorporating image topological property (NC). We present the newly proposed NC-Cut algorithm [16] for IIS in this section. NC-Cut models IIS by utilizing both image appearance models and NC, and balances their contributions by using the average confidence of connectedness. NC can explore the topological structure of image regions and is not sensitive to user interactions. NC-Cut generates the NC maps and NC forest of an image by expanding outward from the background regions. NC is not defined on the appearance models initialized by user interaction and produces quite informative NC maps and NC forest. By incorporating NC and image appearance models, the proposed NC-Cut requires much less user interaction than the seed-based methods, and is less sensitive to initial ROI than the existing ROI-based methods. The flowchart of the proposed NC-Cut method is shown in Fig. 3.1.

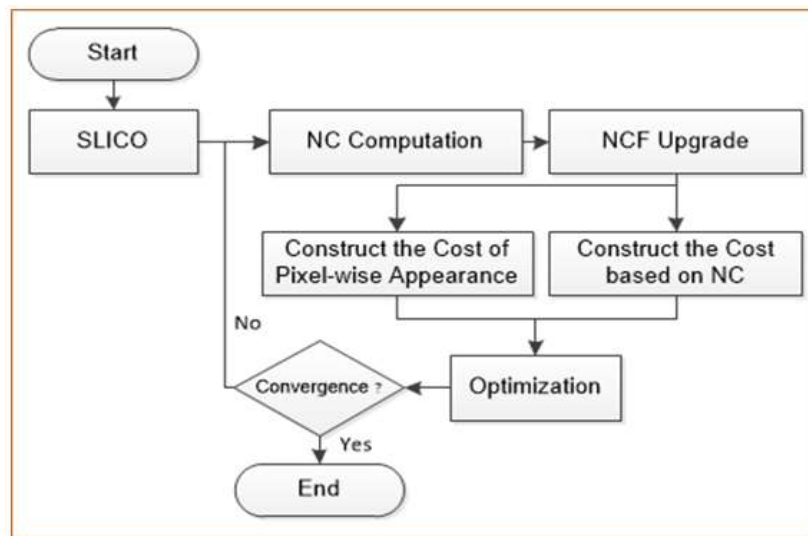


Fig. 3.1. Flowchart of NC-Cut.

### 3.3 NC Computation for Image Regions

The Neutro-connectedness (NC) algorithm discussed in section 2.3 is applied to calculate the NC maps and NC forests for image. Firstly, an image is partitioned into small regions by using the zero-parameter version of SLIC (SLICO) [34]; every image regions are treated as a data points; and for a given region  $p$ , all the regions shares common boundary with  $p$  are viewed as  $p$ 's neighbors.  $\mu_T$  is calculated using Eq. (26), and  $h(p)$  is defined by

$$h(p) = \frac{1}{n_1} \sum_{i=1}^{n_1} (f_{std}(i) \times f_{sobel}(i)) \quad (26)$$

where  $n_1$  is the number of the pixels of region  $p$ , and  $f_{std}(i)$  and  $f_{sobel}(i)$  are the normalized local standard deviation and sobel filter output at point  $i$ , respectively.

Fig. 3.2 shows the results of NC computation of the natural images. All the regions outside ROI (red polygon) are the background seeds used to initialize  $x$  in Algorithm 2.1; the forests, NCFs, are shown in the corresponding T maps. As shown in the second and the fourth columns of Fig. 3.2, all trees are rooted from  $x$ ; the T value of a node is less than or equal to that of its parent node; the object regions have low T values; however, some background regions may also have low T values if they are isolated.

### 3.4 NC-Cut Formulation

Let  $S^p = \{s_i^p \in \{0, 1\}\}_{i=1}^{N^p}$  be a group of binary labels for the pixels: labels **0** and **1** are for pixels in background and object, respectively; Graph  $G_{nNCF}$  is built on the modified NC forest, and  $G_A$  is constructed as the same as that in [26]. The Neutro-Connectedness Cut (NC-Cut) is formulized as

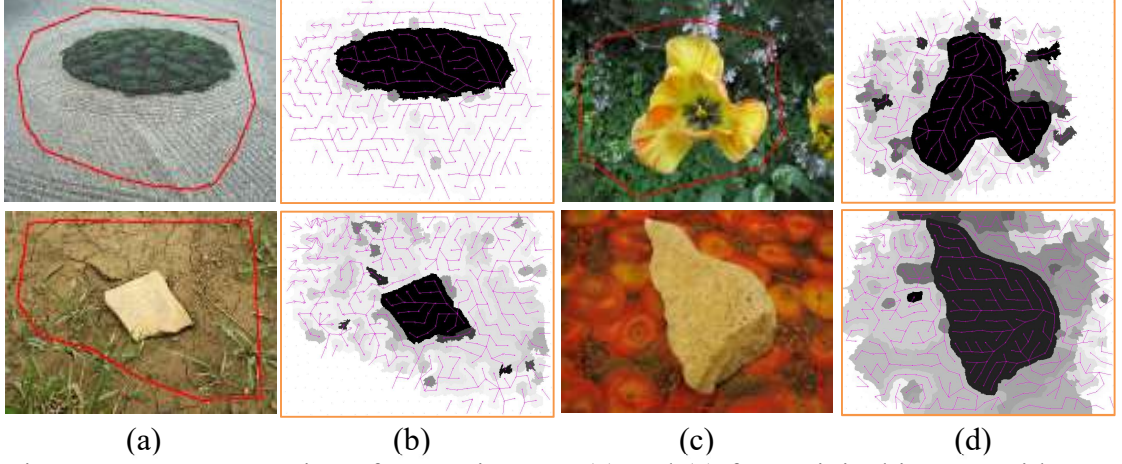


Fig. 3.2. NC computation of nature images. (a) and (c) four original images with user specified ROIs (red polygons); (b) and (d) NCFs of the maps of the degree of truth of NC for each region ( $T_i$  map).

$$\min E(S^p, \theta^A, w) = E^{GA}(S^p, \theta^A) + \gamma E^{G_{nNCF}}(S^p, w^p) \quad (27)$$

In Eq. (27), the cost function  $E$  is defined based on both appearance and topological properties;  $E^{GA}$  takes the form of Grabcut's cost function [26] and defines the cost according to the region and boundary properties;  $E^{G_{nNCF}}$  defines the cost of a cut on  $G_{nNCF}$ ;  $w^p$  defines the weights of t-links (terminal links) and n-links (neighborhood links) of  $G_{nNCF}$ ;  $\gamma$  controls the contribution of  $E^{G_{nNCF}}$ , and is defined by

$$\gamma = e^{-(1-\bar{C})^2/(2\delta_\gamma^2)} \quad (28)$$

where  $\bar{C}$  is the mean value of the confidences of connectedness of all regions;  $\delta_\gamma$  is the standard deviation; and  $\theta^A$  is the set of object and background GMM parameters defined by

$$\theta^A = \left\{ (\pi(k, s), \mu(k, s), \Sigma(k, s)) \mid k = 1, \dots, K, s \in \{0, 1\} \right\} \quad (29)$$

In Eq. (29),  $K$  is the number of components of object (or background) GMM;

$\pi(k, s)$ ,  $\mu(k, s)$ , and  $\Sigma(k, s)$  are the Gaussian mixture weight, mean and covariance matrices of the  $k$ th GMM component for object ( $s = 1$ ) or background ( $s = 0$ ), respectively.

Let  $G_{nNCF} = (\mathcal{V}, \mathcal{E})$  be a graph with vertex set  $\mathcal{V}$  (regions) and edge set  $\mathcal{E}$  defined on the nNCF. The edge set  $\mathcal{E}$  is defined as

$$\mathcal{E} = \underbrace{\{(r, t) | r \neq t \text{ and } (np_{re_r} = t \text{ or } aux_r = t)\}}_{\mathcal{E}_n: n\text{-lin}} \cup \underbrace{\{(r, 0)\} \cup \{(r, 1)\}}_{\mathcal{E}_t: t\text{-links}}, r = 1, 2, \dots, N \quad (30)$$

where  $np_{re_r}$  is the parent node of the  $r$ th region, and  $aux_r$  is the region having an auxiliary edge with the  $r$ th region in nNCF. Let  $w(r, t)$  be the nonnegative weight for each edge  $(r, t) \in \mathcal{E}$  of graph  $G_{nNCF}$ . A cut  $C$  is a subset of  $\mathcal{E}$ , which partitions the vertex set into two disjoint parts. The cost of cut  $C$  is the sum of the weights of the edges in  $C$ , and the optimal cut will have the minimal cost.

We introduce the local connectedness constraint (C1) to the cut  $C$ : let  $(r, t) \in \mathcal{E}$  and  $t = np_{re_r}$ , if node  $r$  is labeled as 0 (background), the label of node  $r$ 's parent node  $t$  should also be 0. If node  $t$  is the parent node of node  $r$ , there will be four possible labeling schemes (Fig. 3.3). The costs of the four possible cuts are

$$\begin{aligned} |C_a| &= w(r, \mathbf{1}) + w(t, \mathbf{0}) + w(r, t), \\ |C_b| &= w(r, \mathbf{0}) + w(t, \mathbf{1}) + w(r, t), \\ |C_c| &= w(r, \mathbf{1}) + w(t, \mathbf{1}), \text{ and} \\ |C_d| &= w(r, \mathbf{0}) + w(t, \mathbf{0}). \end{aligned} \quad (31)$$

As shown in Fig. 3.3, the cuts in Figs. 3.3 (b) - (d) satisfy C1, but Fig. 3.3 (a) does not. In order to avoid the cut in Fig. 3.3 (a), the optimal cut  $C_k$  must satisfy

$$\begin{aligned} |C_k| &= w(r, s_r) + w(t, s_t) + |s_r - s_t|w(r, t) \\ &< w(r, \mathbf{1}) + w(t, \mathbf{0}) + w(r, t) = |C_a| \end{aligned} \quad (32)$$

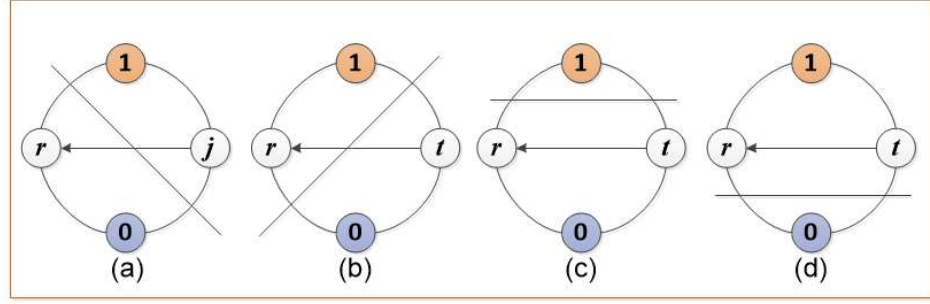


Fig. 3.3. Four possible labeling schemes (cuts) for two adjacent nodes in NCF. (a) node  $r$  is labeled as  $\mathbf{0}$  and  $t$  as  $\mathbf{1}$ ; (b) node  $r$  is labeled as  $\mathbf{1}$  and  $t$  as  $\mathbf{0}$ ; (c) both  $r$  and  $t$  are labeled as  $\mathbf{0}$ ; and (d) both  $r$  and  $t$  are labeled as  $\mathbf{1}$ .

The weights of t-links in  $G_{nNCF}$  are defined by

$$w(r, s_r) = \begin{cases} -\log T_r^{bkg}, & \text{if } s_r = \mathbf{1} \\ -\log(1 - T_r^{bkg}), & \text{if } s_r = \mathbf{0} \end{cases}, r = 1, 2, \dots, N \quad (33)$$

where  $T_r^{bkg}$  is the degree of the truth of connectedness between the  $r$ th region and the seed regions in background; the weights of n-links are defined by

$$w(r, t) = \begin{cases} \lambda e^{-(T_r^{bkg} - T_t^{bkg})^2 / (2\delta_{NC}^2)}, & \text{if } t = npre_r \\ \lambda, & \text{if } t = aux_r \\ 0, & \text{otherwise} \end{cases} \quad (34)$$

where  $\delta_{NC}$  is set as 0.1 by experiment, and  $\lambda$  is a fixed value larger than  $\max\{w(r, s_r) | r = 1, 2, \dots, N\}$ .

**Theorem 1.** Let  $G_{nNCF} = (\mathcal{V}, \mathcal{E})$  be a graph constructed according to the background Neutro-Connectedness. If the edge weights  $w$  are defined by Eqs. (33) and (34), then there always exists a local cut satisfying C1.

*Proof* Let  $t$  be the parent node of  $r$  in a background NCF. Then  $1 \geq T_t \geq T_r \geq 0$ .

If  $T_t > T_r$ , we get  $w(r, \mathbf{1}) > w(t, \mathbf{1})$  and  $w(t, \mathbf{0}) > w(r, \mathbf{0})$ ,

$$\text{therefore } |C_b| < |C_a|;$$

If  $T_t = T_r$ , we have



$$w(r, \mathbf{1}) = w(t, \mathbf{1}), w(r, \mathbf{0}) = w(t, \mathbf{0}) \text{ and } w(r, t) = \lambda,$$

$$\text{therefore } |C_c| = w(r, \mathbf{1}) + w(t, \mathbf{1}) = 2w(r, \mathbf{1})$$

$$< w(r, \mathbf{1}) + w(r, \mathbf{0}) + \lambda = |C_a| \text{ and}$$

$$|C_d| = w(r, \mathbf{0}) + w(t, \mathbf{0}) = 2w(r, \mathbf{0})$$

$$< w(r, \mathbf{1}) + w(r, \mathbf{0}) + \lambda = |C_a|$$

Hence, there always exists a local cut whose cost is smaller than  $|C_a|$ , i.e., C1 is satisfied.

If  $(r, t) \in \mathcal{E}$  and  $t = aux_r$ , it means that  $r$  and  $t$  are two object regions and  $(r, t)$  is an auxiliary edge produced by the linking operation, edge  $(r, t)$  has high weight ( $w(r, t) = \lambda$ ); therefore, similar to the second situation ( $T_t = T_r$ ) in the above proof, a local cut tends to assign label  $\mathbf{1}$  to both  $r$  and  $t$ , which enforces label consistency to object regions with auxiliary edge. The computation of NC and NCF, and construction of  $G_{nNCF}$  are based on image regions to prevent the high time and memory cost of pixel-wise NC computation. However, as shown in Eq. (14), the cost function of the NC-Cut is formulated on image pixels to avoid assigning a uniform label to all pixels in an inhomogeneous region. Therefore, we approximate the NC of pixel by Eqs. (33) and (34). The pixel-wise cost function  $E^{G_{nNCF}}$  of  $G_{nNCF}$  is defined by

$$E^{G_{nNCF}}(S^p, w^p) = \left( \sum_{i=1}^{N^p} w^p(i, s_i^p) + \eta \sum_{i=1}^{N^p} \sum_{j \in N_i} |s_i^p - s_j^p| w^p(i, j) \right) \quad (35)$$

In Eq. (35),  $w^p(i, s_i^p)$  defines the weight of the t-link between the  $i$ th pixel and  $s_i^p$  (0 or 1); and  $w^p(i, j)$  defines the weight of n-link between the  $i$ th and  $j$ th pixels. If the  $i$ th pixel is in the  $r$ th region, then  $w^p(i, s)$  is given by

$$w^p(i, s_i^p) = w(r, s_i^p), \quad (36)$$

where  $w(r, s_i^p)$  is defined in Eq. (20); and  $w^p(i, j)$  is defined by

$$w^p(i, j) = \begin{cases} \lambda, & \text{if } R(i) = R(j) \\ w(R(i), R(j)), & j \in N_i \text{ and } (R(i), R(j)) \in \mathcal{E}_n \\ 0, & \text{otherwise} \end{cases} \quad (37)$$

where  $N_i$  is the set of  $i$ 's adjacent pixels, and  $R(i)$  is the index of the region including the  $i$ th pixel.  $E^{GA}$  is defined as [26]

$$E^{GA}(S^p, \theta^A) = \sum_{i=1}^{N^p} -\log(p_G(x_i, \theta^A, s_i^p)) + \eta \sum_{i=1}^{N^p} \sum_{j \in N_i} \frac{|s_i^p - s_j^p| e^{\beta \|x_i - x_j\|^2}}{D(i, j)} \quad (38)$$

where  $x_i$  is the color feature (RGB) of the  $i$ th pixel,  $\eta$  is set as 50; the constant  $\beta$  is set in the same way as in [26];  $D(i, j)$  is the Euclidean distance between the  $i$ th and the  $j$ th pixels; and  $p_G$  outputs the possibility of the  $i$ th pixel belonging to the object or background, and is defined by [26]

$$p_G(x_i, \theta^A, s_i^p) = \max \left\{ \pi(k, s_i^p) \mathcal{N}(\mu(k, s_i^p), \Sigma(k, s_i^p)) \right\}, k = 1, 2, \dots, K \quad (39)$$

where  $\mathcal{N}(\mu(\cdot), \Sigma(\cdot))$  is a multi-dimensional Gaussian distribution with mean vector  $\mu$  and covariance matrices  $\Sigma$ ;  $\pi(k, s_i^p)$ ,  $\mu(k, s_i^p)$ , and  $\Sigma(k, s_i^p)$  are the Gaussian mixture weight, mean and covariance matrices of the  $k$ th GMM component for object ( $s_i^p = 1$ ) pixel or background ( $s_i^p = 0$ ) pixel, respectively. The cost function in Eq. (27) can be rewritten as

$$\begin{aligned} E(S^p, \theta^A, w) &= E^{GA}(S^p, \theta^A) + \gamma E^{G_{NN}}(S^p, w) \\ &= \sum_{i=1}^{N^p} \left( \gamma w^p(i, s_i^p) - \log(p_G(x_i, \theta^A, s_i^p)) \right) \\ &\quad + \eta \sum_{i=1}^{N^p} \sum_{j \in N_i} |s_i^p - s_j^p| \left( \gamma w^p(i, j) + \frac{e^{\beta \|x_i - x_j\|^2}}{D(i, j)} \right) \end{aligned} \quad (40)$$

### 3.5 NCF Update

The NC computation algorithm, Algorithm 2.1, outputs a background Neutro-Connectedness forest (NCF), in which the root of every tree is from the background regions. As shown in Figs. 3.2(b) and (d), all object regions have quite low connectedness to background regions, and are on the same tree.

However, as shown in Figs. 3.2(b) and (d), some background regions may have low connectedness if they are not connected to the initial background regions. The segmentation method only using the background NC cannot handle these isolated regions. To cope with such problem, we update NCF by integrating pruning and linking operations.

On every tree of the NCF, the leaf nodes (regions) have the lowest connectedness (T value) to their roots (background seeds), and have the highest possibility to be object or isolated background regions; consequently, the candidate object and background regions are defined by

$$P^{obj} = \{r \mid r \text{ is a leaf region in } NCF^{bkg} \text{ and } T_r^{bkg} < \frac{1}{N} \sum_{i=1}^N T_i^{bkg}, \text{ and } r \notin B\} \quad (41)$$

and

$$P^{bkg} = \{r \mid r \text{ is a leaf region in } NCF^{bkg} \text{ and } T_r^{bkg} < \frac{1}{N} \sum_{i=1}^N T_i^{bkg} \text{ and } r \in B\} \quad (42)$$

respectively, where  $T_r^{bkg}$  is the degree of the truth of connectedness between the  $r$ th region and the background seed regions, the threshold for filtering the leaf regions is set as the mean of all regions' background connectedness ( $\frac{1}{N} \sum_{i=1}^N T_i^{bkg}$ ), and set  $B$  includes all regions of high similarity with background seed regions and is given by

$$B = \{r \mid f(r) = e^{-\frac{(p^{bkg}(m(r)) - u_B)^2}{2\delta_B^2}} > \varepsilon\} \quad (43)$$

where  $p^{bkg}(\cdot)$  is the background GMM distribution learned from  $SRs^{bkg}$ ,  $m(r)$  is the mean of color features (RGB) of the  $r$ th region,  $u_B$  is the mean of  $p^{bkg}(\cdot)$  of the regions in  $SRs^{bkg}$  and is defined as  $(1/n^{bkg}) \sum_{r \in SRs^{bkg}} p^{bkg}(m(r))$  where  $n^{bkg}$  is the size of  $SRs^{bkg}$ , and  $\delta_B$  and  $\varepsilon$  are the standard deviation and the threshold, respectively.

The candidate object regions  $P^{obj}$  include all the leaf regions in  $NCF^{bkg}$  having low  $T$  value and low similarity with  $SRs^{bkg}$ , and the candidate isolated background regions  $P^{bkg}$  are the leaf regions with low connectedness but high similarity with  $SRs^{bkg}$ .

As shown in Fig. 3.4 (c), 29 of 30 candidate regions of the object (indicated by yellow points) determined by Eq. (41) belong to the object; and all candidate regions of isolated background (indicated by green points) determined by Eq. (42) are in the background. In Fig. 3.4(e), after five iterations of Algorithm 3.1(section 3.6), all candidate object regions are correctly in the object; and there is no candidate background regions because no region satisfies Eq. (42).

The NCF is updated by using the following two operations:

1) Pruning. Disconnect the edge between any isolated background region and its parent node by resetting its parent and root nodes to itself (Eqs. (43) and (44)).

$$npre_r = \begin{cases} r, & r \in P^{bkg} \\ pre_r, & otherwise \end{cases} \quad (44)$$

$$nrt_r = \begin{cases} r, & r \in P^{bkg} \\ rt_r, & otherwise \end{cases} \quad (45)$$

In Eqs. (44) and (45),  $npre_r$  and  $nrt_r$  denote the new parent node and the new root node of the  $r$ th region.

2) Linking. Add an *auxiliary edge* to each pair of adjacent object regions located on the same tree (Eq. (46)).

$$aux_r = \begin{cases} g, g \in \mathbb{N}(r), g \in P^{obj}, \text{ and } rt_r = rt_g \\ r, \text{ otherwise} \end{cases} \quad (46)$$

In Eq. (46),  $\mathbb{N}(r)$  denotes all the adjacent regions of the  $r$ th region.

The pruning operation is applied for breaking the link between an isolated background region and its parent, which will exclude the isolated background regions from the segmentation results. The linking operation connects object nodes by adding *auxiliary edges*, which will enforce label consistency to adjacent object nodes. The modified NCF (nNCF) is defined by

$$\text{nNCF} = \{(npre_r, nrt_r, aux_r)\}_{r=1}^N \quad (47)$$

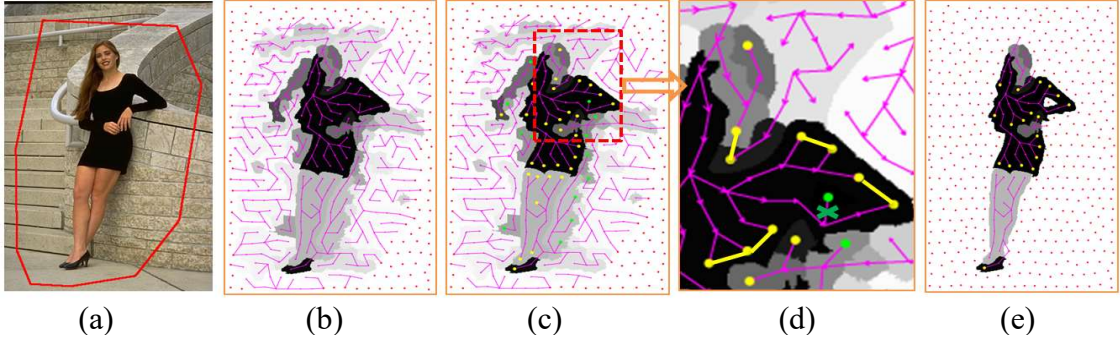


Fig. 3.4. Candidate object and background regions. (a) Original image with a loose ROI (red polygon); (b) background NCF (magenta arrows); (c) the object (yellow points) and background (green points) regions on  $T_i$  map; (d) the pruning (green cross) and linking (yellow edges) operations of the region in the red dashed rectangle in (c); (e) the candidate object and background regions after the fifth iteration of Algorithm 3.1.

We use Figs. 3.4(c) and (d) to demonstrate how to update the original NCF. In Fig. 3.4(d), the yellow line segments indicate the auxiliary edges added by the linking operation, and the green cross mark indicates that the edge will be removed by the pruning operation.

---

**Algorithm 3.1: Iterative NC cut**


---

Inputs: image  $x = \{x_i\}_{i=1}^{N^p}$ , and a user specified ROI

Outputs:  $S^p = \{s_i^p \in \{0,1\}\}_{i=1}^{N^p}$

1: Initialization:

$$s_i^p = \begin{cases} 1, & \text{if } x_i \text{ is in the ROI} \\ 0, & \text{otherwise} \end{cases}, i = 1, \dots, N^p$$

generate image regions  $R = \{R_i\}_{i=1}^N$  using SLICO,

compute the dissimilarity matrix ATs and

indeterminacy matrix AIs

2: Learning the object and background GMMs'

parameters  $\theta^A$

3: Update the SRs

4: Compute background NC and NCF using Algorithm 1

5: NCF update

6: Update weights of links  $w^p$  using Eqs. (23) and (24)

7: Apply max-flow algorithm to solve Eq. (27)

8: Repeat steps 1 to 6 until convergence

---

### 3.6 Optimization

The optimization of the proposed NC-Cut is conducted iteratively (Algorithm 3.1), and estimates appearance models and NC jointly.

In step 2, the parameters of appearance models (GMMs) are estimated. For a given foreground ( $s = 1$ ) or background ( $s=0$ ) GMM,  $FB(k, s) = \{x_i | k_i = k, s_i^p = s\}$  defines pixels for the  $k$ th GMM component; the mixture weights are  $\pi(k, s) = |FB(k, s)| / \sum_{k=1}^K |FB(k, s)|$ ; the mean  $\mu(k, s)$  is defined as the sample mean  $\mu(k, s) = \sum_{x_i \in FB(k, s)} x_i / |FB(k, s)|$ ; the covariance matrices  $\Sigma(k, s)$  are estimated as the covariance of pixels' RGB values in  $FB(k, s)$ .

In step 3, the SRs set is updated by using the segmentation result ( $S^p$ ) of the previous iteration: the regions with more than 80% pixels labeled as 0s will be added to SRs; in step 4, Algorithm 2.1 generates the NC and NCF based on image regions; in step 5, we

apply the object and background regions to update the background NCF; in step 6, the pixel-wise weights of t-links and n-links are updated by using Eqs. (36) and (37); and the cost function is optimized by using the max-flow algorithm in step 7. All the steps will repeat until convergence (no change of the segmentation result).

User editing. If an interactive image segmentation approach cannot generate a satisfied result, further user editing is needed [12, 26]. For Algorithm 2, the user editing is to brush the wrongly labeled object and background superpixels and to update the GMMs and SRs; then the entire iterations (steps 2-8) of are applied. Notice that the image region set  $R$ , matrix ATs and AIs, and previous segmentation could be re-used.

### 3.7 Dataset, Metrics, and Parameter Settings

The performance of the proposed NC-Cut method is validated using two datasets. The first dataset (DS1) is the Grabcut [26] dataset which contains 50 images from the Berkley image dataset (BSD300) [35]. The second dataset (DS2) includes 215 images from MSRA [36] dataset. The manually marked regions of objects are used as the ground truth (GT).

The intersection-over-union (IoU) score [35], Error Rate (ERR), Rand Index (RI) [20], Global Consistency error (GCE) [21], and Boundary Displacement Error (BDE) [22] are commonly employed to assess the performance of the interactive segmentation methods. The IoU score for the object/background is defined as the ratio of the number of correctly labeled object/background pixels to the number of pixels labelled with the object/background in either the ground truth or the segmentation result. The average IoU over object and background are employed to evaluate the overall performance. The ERR counts

the percentage of wrongly labeled pixels in ROI. The RI computes the fraction of pixel pairs having consistent labels in both the segmented result and the ground truth; which takes value in  $[0, 1]$ , value 1 indicates that the segmentation result and the ground truth are exactly the same, and 0 indicates that they disagree on every pixel pairs. The GCE measures the consistency between the segmentation result and the ground truth; it takes value in  $[0, 1]$ , and the value close to 0 indicates high accuracy. The BDE computes the average displacement of boundary pixels between the segmentation result and the ground truth; the displacement error of a boundary pixel is defined as the Euclidean distance between the pixel and its closest pixel on the boundary of the ground truth.

We compare the proposed NC-Cut algorithm with four state-of-the-art interactive segmentation algorithms: Grabcut [26], One-Cut [28], MILCut [30], and pPBC [31]. The parameters of Grabcut [26], MILCut [30] and pPBC [31] are adopted from the related publications. In One-Cut [28], the number of color bins is set as 1283, the weight of smoothness is set as 5. Here, we would like to acknowledge the authors of MILCut, One-Cut and pPBC for providing the source code or executable program. The code of the Grabcut is available online (<http://grabcut.weebly.com/code.html>). All experiments are performed on windows-based PC equipped with a dual-core processor (2GHz) and 4GB memory.

### 3.8 Experimental Results of Interaction Dependence

The proposed NC-Cut method is compared with other four ROI-based interactive methods: Grabcut [26], One-Cut [28], MILCut [30] and pPBC [31].

Fig. 3.5 (a) shows five natural images; each image has one loose ROI and one tight ROI specified by user.



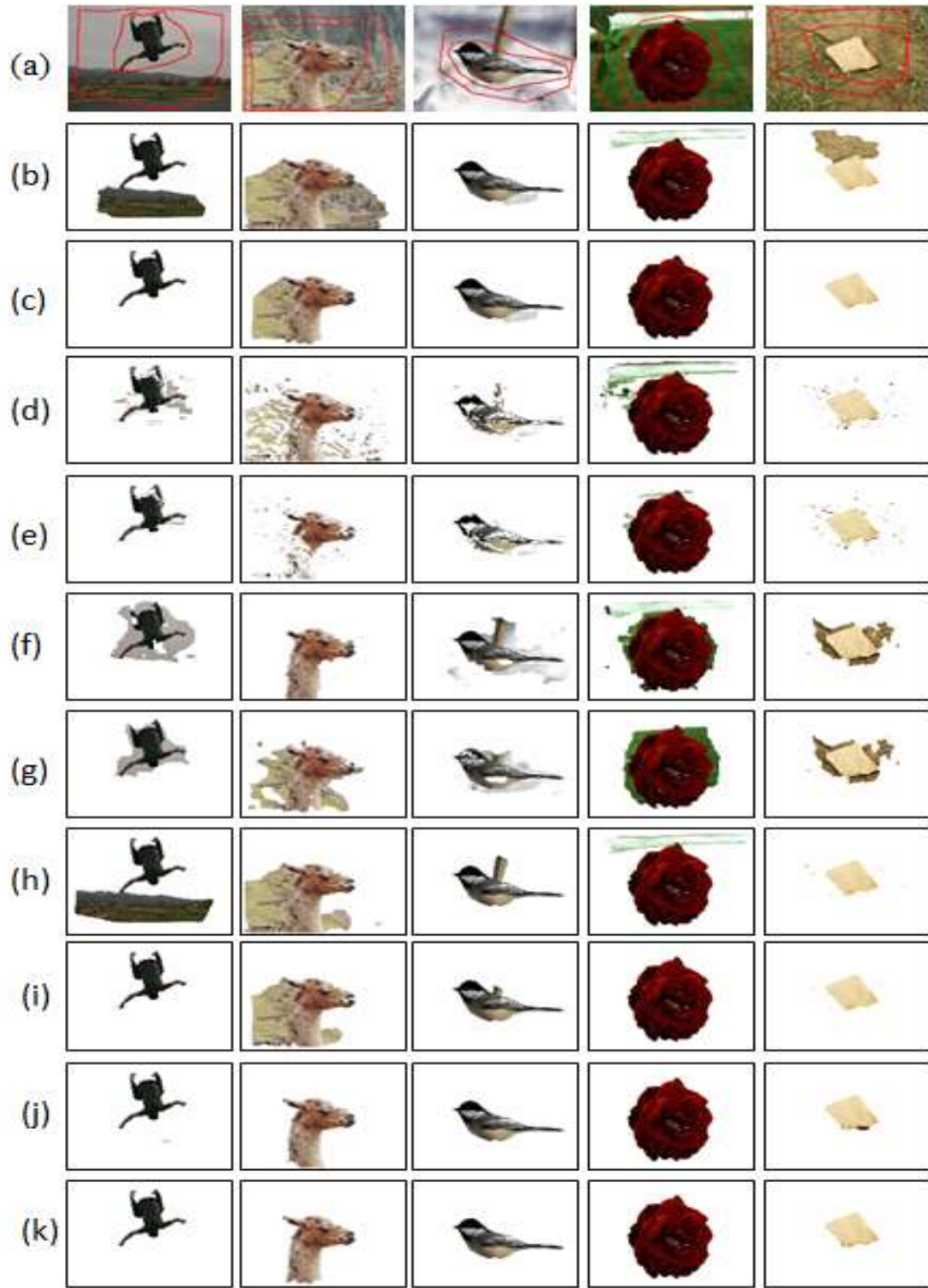


Fig. 3.5. Five examples. (a) Five images and user-specified ROIs (tight and loose); (b) and (c) results of Grabcut; (d) and (e) results of One-Cut; (f) and (g) results of MILCut; (h) and (i) results of the pPBC; (j) and (k) results of the proposed NC-Cut.

Fig. 3.5(b) demonstrates that when the ROIs are loose, the Grabcut method wrongly labels many pixels; Fig. 3.5(c) shows that when the ROIs are tight, the Grabcut produces quite accurate results. As shown in Figs. 3.5(d) and (e), One-Cut is less sensitive to the initial ROIs than Grabcut, and can obtain better results than Grabcut on the last two images with loose ROIs; however, it cannot generate better results than Grabcut on the images with complicated object appearance (the third and fourth images).

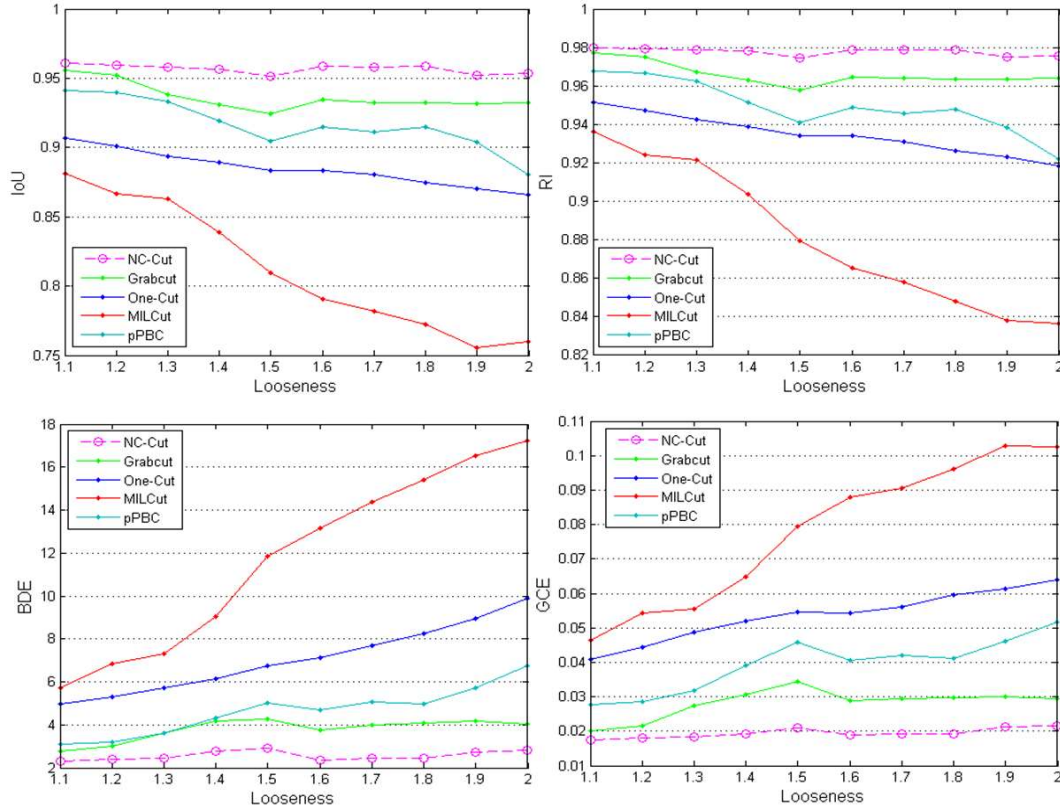


Fig. 3.6. Segmentation performance according to different ROI looseness.

The MILCut method may not always produce better results using tight ROI than that using loose ROI (third image), and Figs.3.5(f) and (g) demonstrate that MILCut is more sensitive to the initial ROI than Grabcut and One-Cut. In Figs. 3.5(h) and (i), the

pPBC obtains better results than the other three methods, but it is still sensitive to the initial ROI; while the proposed NC-Cut method can produce accurate results (Figs. 3.5(j) and (k)) for all the images, and generates almost the same segmentation results using either tight or loose ROIs.

To evaluate the five methods' level of sensitivity to different ROIs quantitatively, we generate 10 groups of bounding boxes with different looseness automatically. We use the bounding box of the ground truth as the baseline, and set its looseness to 1; then move the four sides of the bounding box toward image borders to increase the looseness. The amount of move is proportional to the margin between the side and the image border. The looseness of a bounding box is defined as the ratio of area of the new bounding box to the area of the baseline bounding box. Twenty-eight images having bounding box with looseness at least 2 are selected from the two datasets. As shown in Fig.3.6, the proposed NC-Cut is much less sensitive to the looseness of ROI than the other four methods.

### 3.9 Overall Performance

The proposed NC-Cut and other four state-of-the-art ROI-based methods are compared by utilizing the two datasets with predefined tight ROIs and loose ROIs. We also compare the proposed method without using the indeterminacy (NC-Cut0) with the proposed NC-Cut to demonstrate the impacts of the indeterminacy on segmentation performance. We specify loose ROIs in the original images by drawing polygons to include more background pixels. As shown in Tables 3.1 and 3.2, using datasets DS1 and DS2, Grabcut obtains better average results with tight ROIs than those with loose ROIs; using dataset

DS2, the average performances of One-Cut and MILCut drop dramatically when the ROIs change from tight to loose.

Table 3.1. Average performance on dataset DS1

|                     | Tight ROIs |       |      |       | Loose ROIs |       |      |       |
|---------------------|------------|-------|------|-------|------------|-------|------|-------|
| Methods             | RI         | GCE   | BDE  | IoU   | RI         | GCE   | BDE  | IoU   |
| Grabcut             | 0.94*      | 0.04* | 7.7  | 0.91* | 0.90       | 0.06  | 12.2 | 0.85  |
| One-Cut             | 0.88       | 0.06  | 10.4 | 0.80  | 0.88       | 0.08  | 12.7 | 0.80  |
| MILCut              | 0.85       | 0.12  | 16.8 | 0.80  | 0.87       | 0.11  | 13.2 | 0.82  |
| pPBC                | 0.94*      | 0.05  | 6.8* | 0.91* | 0.92       | 0.06  | 8.8  | 0.83  |
| NC-Cut <sub>0</sub> | 0.91       | 0.05  | 14.1 | 0.85  | 0.91       | 0.05* | 12.1 | 0.85  |
| NC-Cut              | 0.94*      | 0.05  | 7.3  | 0.91* | 0.94       | 0.05* | 8.5* | 0.90* |

\* indicates the best result(s) in the same column; NC-Cut<sub>0</sub> is the proposed method without using the indeterminacy.

Table 3.2. Average performance on dataset DS2

|                     | Tight ROIs |       |      |       | Loose ROIs |       |      |       |
|---------------------|------------|-------|------|-------|------------|-------|------|-------|
| Methods             | RI         | GCE   | BDE  | IoU   | RI         | GCE   | BDE  | IoU   |
| Grabcut             | 0.98*      | 0.02* | 1.9  | 0.97* | 0.96       | 0.03  | 3.9  | 0.94  |
| One-Cut             | 0.94       | 0.05  | 4.5  | 0.92  | 0.88       | 0.09  | 12.2 | 0.86  |
| MILCut              | 0.89       | 0.08  | 8.5  | 0.86  | 0.73       | 0.17  | 24.7 | 0.67  |
| pPBC                | 0.98*      | 0.02* | 2.1  | 0.97* | 0.93       | 0.04  | 6.1  | 0.91  |
| NC-Cut <sub>0</sub> | 0.97       | 0.02* | 2.4  | 0.96  | 0.97       | 0.02* | 2.3* | 0.96* |
| NC-Cut              | 0.98*      | 0.02* | 1.8* | 0.97* | 0.98*      | 0.02* | 2.3* | 0.96* |

\* indicates the best result(s) in the same column; NC-Cut<sub>0</sub> is the proposed method without using the indeterminacy.

The proposed NC-Cut method outperforms Grabcut, One-Cut, MILCut and pPBC in all metrics (IoU, RI, GCE and BDE) using the two datasets with loose ROIs; and obtains similar results with Grabcut and pPBC, and much better results than One-Cut and MILCut using tight ROIs. The average IoU, RI, GCE and BDE of the NC-Cut using the two datasets are almost the same with both the loose or tight ROIs, which implies that the proposed

approach is not sensitive to the sizes of the initial ROIs; and this is the advantage which cannot be demonstrated by any existing state-of-the-art methods.

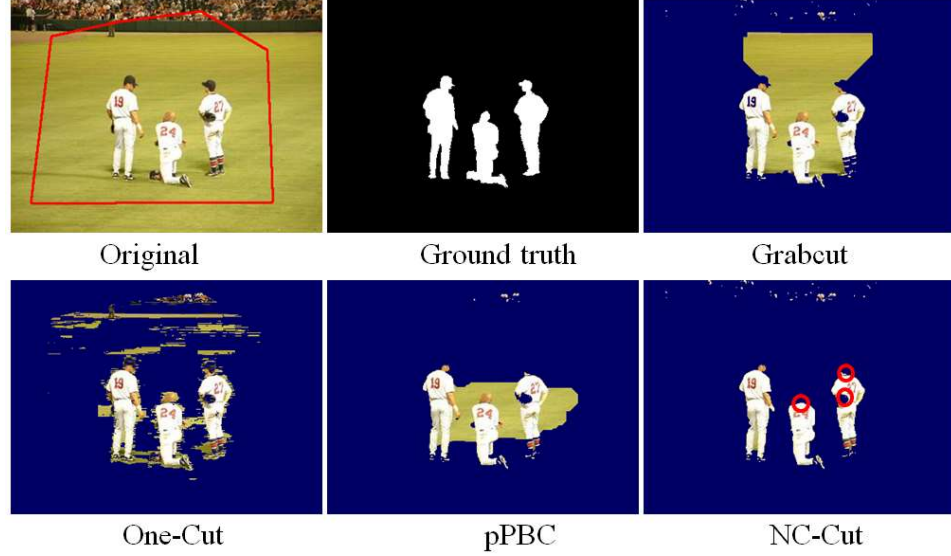


Fig. 3.7. Failure case.

The only difference between  $\text{NC-Cut}_0$  and  $\text{NC-Cut}$  is that the confidence of connectedness ( $C$ ) is not utilized in  $\text{NC-Cut}_0$  (i.e.,  $C = 1$ ). As shown in Table 3.1,  $\text{NC-Cut}_0$  cannot achieve good performance as  $\text{NC-Cut}$  with both the loose or tight ROIs on DS1. Because most images in DS2 have homogenous background, the segmentation performance of  $\text{NC-Cut}_0$  does not degrade much.  $\text{NC-Cut}$  can avoid shrinking problem on many images because of the using of global properties; however, the contribution of the global term  $E^{G_{\text{NCF}}}$  in  $\text{NC-Cut}$  is determined by the average confidences of connectedness. If an image has low level of average confidence of connectedness (small  $\gamma$ ),  $\text{NC-Cut}$  will transfer more control to the appearance term ( $E^{G_A}$ ) which may result in the shrinking problem as Grabcut and Graph cuts on some images (Fig. 3.7). How to solve such problem will be studied in the future.

## CHAPTER 4

### EFFECTIVE INTERACTIVE SEGMENTATION

Effective interactive segmentation (EISeg) provides user with visual clues to guide the interacting process based on Neutro-Connectedness (NC). The boundary connectedness map and NC forest calculated in EISeg can lower the dependence of segmentation performance on the appearance models and can also reduce user interaction greatly by guiding user where to interact can achieve the best segmentation results. The main results of this work have been published in [39].

#### 4.1 Overview

The flowchart and an example of the proposed EISeg method are shown in Fig. 4.1. The EISeg includes three main parts. The first part is the boundary connectedness mapping which computes Neutro-Connectedness (NC) between each image region and boundary regions. The boundary connectedness has two components: boundary connectedness map (BCM) and boundary connectedness forest (BCF). The two components are quite informative to distinct object and background; and we will apply them to provide visual clues for user to determine seeds effectively. The second part is the interaction protocols. The protocols explain the meanings of the BCM and BCF, and define three simple guidelines for user to determine the most suitable the seeds. The EISeg formulation and optimization are in the third part. The EISeg is formulated as energy minimization problem based on GMM appearance models (Grabcut [26]) and boundary connectedness, which will reduce the sensitivity of the proposed method to user interactions. Like NC-Cut and Grabcut, EISeg is optimized iteratively with GMM and boundary connectedness updated in each iteration.

## 4.2 Boundary Connectedness Computation

The boundary connectedness is a topological property between each image region and the regions on image boundary. We calculated boundary connectedness map (BCM) and boundary connectedness forest (BCF) by using Algorithm 2.1; The image regions are produced by using the zero-parameter version of SLIC (SLICO) [34] method, and all regions connected with image boundary are set as boundary seeds.

As shown in Fig. 4.2, the BCM and BCF are shown in one image. The BCM is shown as a grey image; the BCF is illustrated on the BCM as color arrows, and each color indicate one tree.

## 4.3 Protocols for User Interactions

In this section, the interpretations of boundary connectedness map (BCM) and boundary connectedness forest (BCF) are described; and then we define the protocols to guide user interactions.

In EISeg, the boundary regions are viewed as the background seeds. High degree of boundary connectedness indicates the high possibility of one region to be the background, whereas the image region with low degree of connectedness has high possibility to be object. As shown in Fig. 4.1, the BCM is quite informative for distinguish objects from the background. The BCF visually illustrates the topological structure of the BCM. There are three facts of BCF: First, all connected structures located on the same tree, e.g., the flower in Fig. 3.8. Second, every tree in BCF roots in the boundary region set. Third, the further a node is from the root, the less the degree of connectedness between the node

and the root. According to the facts of BCM and BCF, three simple protocols for user interaction are defined as follows.

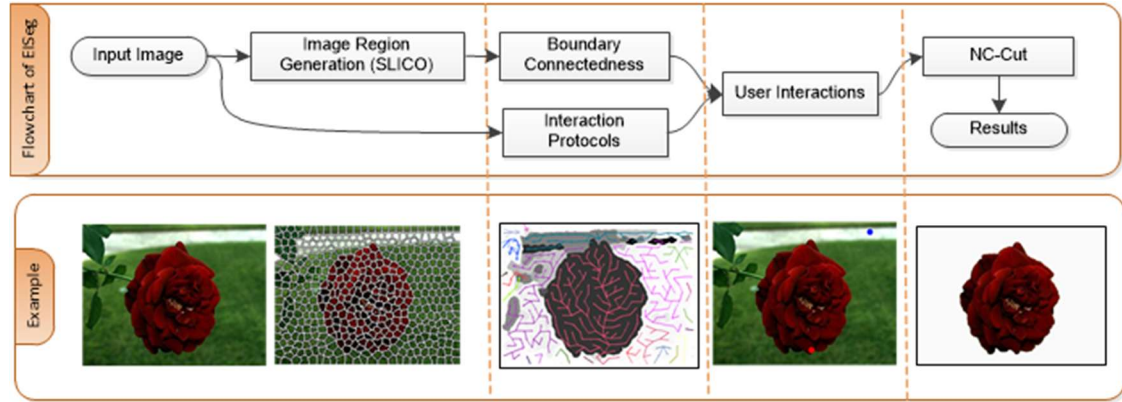


Fig. 4.1. Flowchart of EISeg.

P1: Label isolated background regions with low boundary connectedness as background. If several isolated background regions are on the same subtree, only the root of the subtree needs to be labeled, which reduces both the interaction intensity and the convergence time.

P2: Label the object region which is a child of a background region as the foreground. There may exist more than one such object regions. If the connectedness difference between the object region and background region is large, no need to label the object region.

P3: Label object regions connected to the image boundary as the foreground. In some images, some parts of object are boundary regions, thus we need to exclude these regions from the boundary region for generating meaningful boundary connectedness map.

The three protocols provide user with guidelines about how to interact based on the BCM and BCF.



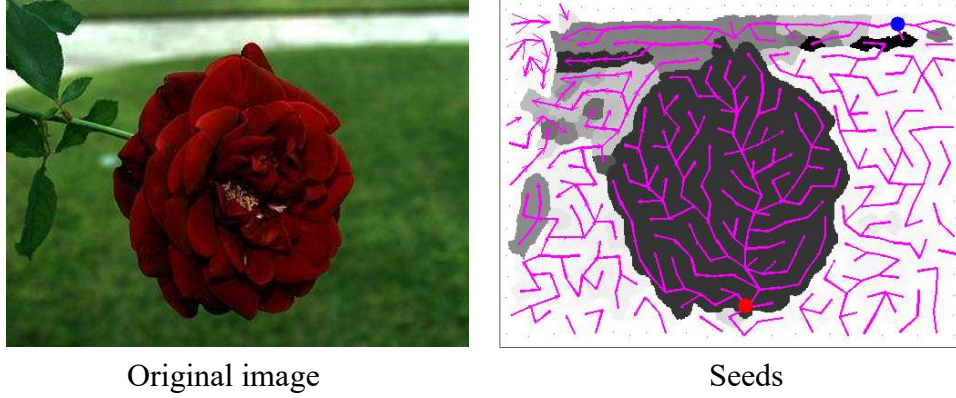


Fig. 4.2. Example of labeling seed regions. The blue point is a background seed selected according to P1; and the red point is an object seed selected based on P2.

Fig. 4.2 demonstrates that it is easy to select seeds by applying the protocols. Let  $F_0$  and  $B_0$  are the sets of indices of user specified object and background regions (seeds), respectively; we extend them by using the BCF:

$$\begin{aligned}
 B &= \{p \text{ and its successors on BCF} \mid p \in B_0\} \cup \{\text{the predecessors of } q \mid q \in F_0\} \\
 F &= \{q \text{ and its successors on BCF} \mid q \in F_0\} - B
 \end{aligned} \tag{48}$$

#### 4.4 EISeg Formulation and Optimization

Let  $x = \{x_i\}_{i=1}^N$  denote the colors of each pixel in an image;  $y = \{y_i \in \{0, 1\}\}_{i=1}^N$  be a group of binary labels for each pixel: labels 0 and 1 are for the pixels in background and object, respectively. The proposed EISeg is formulized as

$$\begin{aligned}
 E(y, \theta, \vartheta, x) &= \sum_{i=1}^N D(x_i, \theta, \vartheta, y_i) + \eta \sum_{(i,j) \in C} S(x_i, x_j, \vartheta, y_i, y_j) \\
 s. t. \quad y_m &= 1, \text{ if } R(m) \in F; y_m = 0, \text{ if } R(m) \in B
 \end{aligned} \tag{49}$$

where  $\theta$  denotes the appearance models of the objects and the background,  $\vartheta$  is the boundary connectedness map,  $\delta_k$  is the Dirac measure,  $C$  is a set of all pairs of neighboring pixel,

the constant  $\eta$  determines the degree of encouraging the smoothness term,  $R(m)$  is the index of the region containing the  $m$ th pixel, and  $D$  and  $S$  define the data and smoothness terms, respectively.

In Eq. (49), the proposed cost function  $E$  is defined based on both appearance ( $\theta$ ) and boundary connectedness map ( $\vartheta$ ); therefore, the solving of this problem will take both appearance and global topological properties jointly.

The data term has two components: (1) the first component calculates the labeling cost according to the region property, and takes the form of Grabcut's cost function [26]; (2) the second component introduces the boundary connectedness to define cost on topological property. The data term is defined by

$$D(x_i, \theta, \vartheta, y_i) = (\gamma - 1) \log(p_G(x_i, \theta, y_i)) - \gamma \log(y_i \vartheta_i + (1 - y_i)(1 - \vartheta_i)) \quad (50)$$

where  $\vartheta_i$  is the boundary connectedness of the  $i$ th pixel, and is assigned as the boundary connectedness value of the  $r$ th superpixel which contains the  $i$ th pixel; Refer to section 3.4 for the definitions of  $\gamma$  and  $p_G$ .

The smoothness term defines the cost on boundary property, and is defined by

$$S(x_i, x_j, \vartheta, y_i, y_j) = |y_i - y_j| \cdot$$

$$\left( \gamma \cdot [i = pre_j] e^{-(\vartheta_i - \vartheta_j)^2 / (2\delta_{NC}^2)} + (1 - \gamma) \cdot \frac{e^{-\beta \|x_i - x_j\|^2}}{d(i, j)} \right) \quad (51)$$

where  $[\cdot]$  is an indicator function taking values 0 and 1;  $pre_j$  is the parent node of the  $j$ th pixel;  $\delta_{NC}$  is selected as 0.1 by experiment;  $d(i, j)$  is the Euclidean distance between the  $i$ th and  $j$ th pixels; and the constant  $\beta$  is set in the same way as in [26].

In Eq. (51), the smoothness term penalizes both the color and connectedness discontinuities of neighboring pixels; the penalty of color discontinuities are calculated on all neighboring pixels, while the connectedness penalties are enforced on the connectedness forest. The cost function of EISeg is similar to that of the NC-Cut; but there are two main differences between EISeg and NC-Cut: first, the user interactions in EISeg are guided by BCM and BCF, while the interactions in NC-Cut is arbitrary; second, in EISeg, the equality constraints are introduced to make the labels specified by user unchanged in future iterations.

---

**Algorithm 4.1: EISeg Optimization**

---

Inputs: image  $x = \{x_i\}_{i=1}^N$ , and sets  $F$ ,  $B$ , BDRs

Outputs:  $y = \{y_i \in \{0,1\}\}_{i=1}^N$

Initialization:

$$y_i = \begin{cases} 1, & \text{if } i \in F, \text{ or } i \notin \text{BDRs} \\ 0, & \text{otherwise} \end{cases} \forall i$$

Optimization:

- 1: Learning the GMMs' parameters  $\theta$
  - 2: Set the regions with more than 80% background pixels to be boundary regions
  - 3: Compute boundary connectedness :  
 $\{\vartheta_i\}_{i=1}^N$  and  $\text{BCF} = \{\text{pre}_i\}_{i=1}^N$
  - 4:  $D(x_i, \theta, \vartheta, 0) = \max(D)$ , if  $R(i) \in F$ ,  
 $D(x_i, \theta, \vartheta, 0) = \min(D)$ , if  $R(i) \in B$ ,
  - 5: Apply max-flow algorithm
  - 6: Repeat steps 1 and 5 until convergence
- 

Like Grabcut and NC-cut, we apply the block-coordinate descent method to minimize the cost function of the proposed EISeg method. The details are illustrated in Algorithm 4.1 which alternates two steps: first, it fixes segmentation, and learns appearance

model ( $\theta$ ) and computes BCM and BCF; second, update segmentation based on new models and parameters. The convergence condition is that the number of pixel with different labels between the outputs of two consecutive iterations is smaller than 0.001 of the number of image pixels.

#### 4.5 Experimental Results

The performance of the newly proposed EISeg method is validated utilizing the NC-Cut dataset [16] including 215 images from MSRA [36]. The manually marked regions of objects are the ground truths (GTs). Traditional interactive segmentation methods mainly focused on the improvement of segmentation models, but ignored the effectiveness of user interaction. Due to the absence of how to interact to achieve better result, those methods have great arbitrariness of user interaction, and good segmentation results can only be achieved by involving intense user interactions, e.g., setting more seeds, or specifying a new ROI to exclude more background regions.

In this section, we will compare EISeg with Grabcut [26] and pPBC [31]. Grabcut and pPBC are two ROI-based methods. In Fig. 4.3, we specify two different ROIs for each of the four original images (Fig. 4.3(a)); the segmentation results of Grabcut and pPBC (Figs. 4.3(b) - (e)) illustrate that different ROIs may result in quite different segmentation performance and user usually has no clue about where to set ROI which can generate the best result. Fig. 4.3(f) shows the seeds specified according to the proposed interaction protocols in EISeg; and only two or three seeds are specified for each image. Fig. 4.3(g) demonstrates that the proposed EISeg can generate quite accurate results based on weak user interaction.

We evaluate the proposed EISeg, Grabcut [26] and pPBC [31] using the NC-Cut dataset [12]. A user specified background and object seeds for each image according to the proposed interaction protocols; and the user specified seeds and all boundary regions are used to initialize all three approaches. Table 4.1 shows that the EISeg outperforms the other two methods on all four metrics; and averagely only 2.3 foreground and 1.8 background seeds are specified per image.

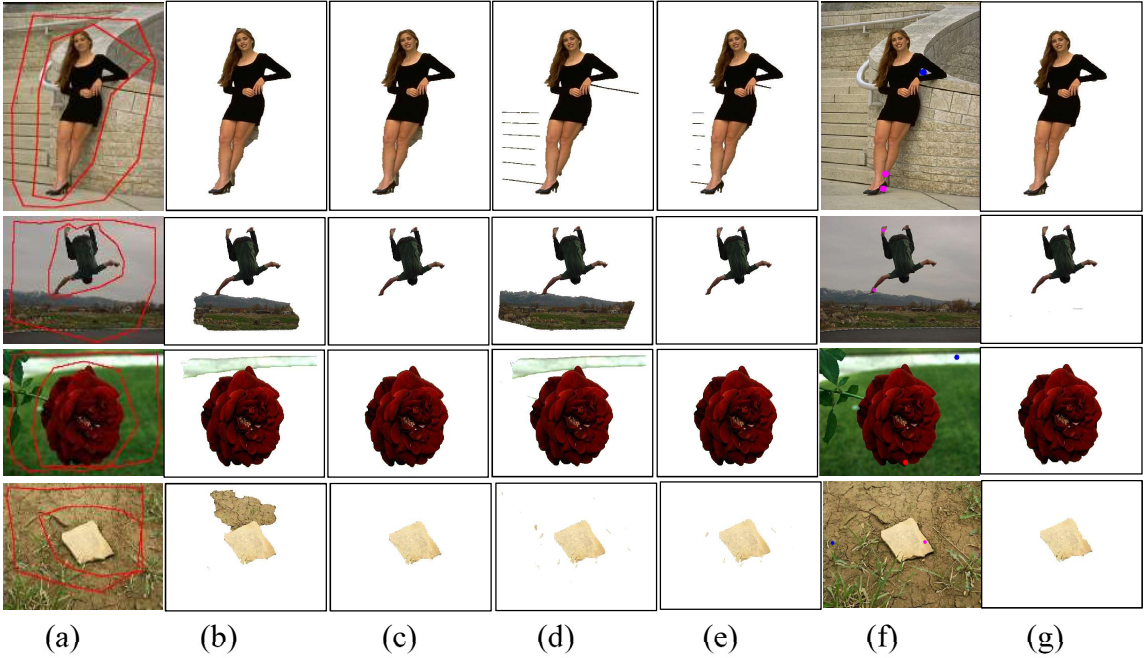


Fig. 4.3. Interaction effectiveness. (a) original images with a loose and a tight ROIs; (b) and (c) results of Grabcut with loose and tight ROIs, respectively; (d) and (e) results of pPBC with loose and tight ROIs respectively; (f) interactions of the proposed EI<sup>2</sup>S method; and (g) results of the EISeg.

Table 4.1. Overall Performance on NC-Cut dataset [16].

| Methods      | ERR(%) | RI   | GCE  | BDE  |
|--------------|--------|------|------|------|
| Grabcut [26] | 8.4    | 0.91 | 0.05 | 10.4 |
| pPBC [31]    | 11.1   | 0.88 | 0.06 | 12.5 |
| EISeg        | 1.1    | 0.98 | 0.02 | 2.1  |

## CHAPTER 5

### NC FOR FULLY AUTOMATIC BUS IMAGE SEGMENTATION

In this chapter, NC is applied to solve the challenges of segmenting medical images with low image quality. The main results have been published in [11, 38, 86].

#### 5.1 Background

Breast cancer occurs in the highest frequency in women among all cancers, and is also one of the leading causes of cancer death worldwide [37]. Scientists do not definitely know what causes breast cancer yet, and only know some risk factors that can increase the likelihood of developing breast cancer: getting older, genetics, radiation exposure, dense breast tissue, alcohol consumption, etc. The key of reducing the mortality is to find signs and symptoms of breast cancer at its early stage by clinic examination. Breast ultrasound (BUS) imaging has become one of the most important and effective modality for the early detection of breast cancer because of its noninvasive, nonradioactive and cost-effective nature; and it is most suitable for large-scale breast cancer screening and diagnosis in low-resource countries and regions.

Computer-Aided Diagnosis (CAD) systems based on B-mode breast ultrasound have been developed to overcome the considerable inter- and intra-variabilities of the breast cancer diagnosis, and have been clinically tested their ability to improve the performance of the breast cancer diagnosis. BUS segmentation, extracting tumor region of a BUS image, is a crucial step for a BUS CAD system. Base on the segmentation results, quantitative features will be calculated to describe tumor shape, size, echo pattern, etc., and be input into a classifier to determine the category of the tumors. Therefore, the precision of

BUS segmentation directly affects the performance of the quantitative analysis and diagnosis of tumors.

Automatic BUS image segmentation study attracted great attention in the last two decades due to clinical demands and its challenging nature, and results in a lot of automatic algorithms. We can classify existing approaches into semi-automatic and fully automatic methods according to with or without user interactions in the segmentation process. In most semi-automatic methods, user needs to specify a region of interest (ROI) containing the lesion, a seed in the lesion, or an initial boundary. Fully automatic segmentation is usually modeled as a top-down framework which models knowledge of breast ultrasound and oncology as prior constraints, and needs no user intervention at all. However, it is quite challenging to develop automatic tumor segmentation approaches for BUS images, due to the low image quality caused by speckle noise, low contrast, weak boundary, and artifacts. Furthermore, tumor size, shape and echo strength vary considerably across patients, which prevent the application of strong priors to object features that are important for conventional segmentation methods.

## 5.2 A Short Review of BUS Image Segmentation Approaches

We classify the BUS image segmentation approaches in four categories: (1) deformable models, (2) graph-based approaches, (3) learning-based approaches, and (4) classical approaches (e.g., thresholding, region growing, and watershed). The four categories dominate BUS segmentation approaches. For more details, refer to [86].

Deformable models (DMs): DMs-based approaches move the curves or surfaces

toward to the object boundary with the influence of forces. They have been studied extensively in BUS image segmentation. According to the ways of representing the curves and surfaces, we can generally classify DMs into two categories: (1) the parametric DMs (PDMs) and (2) the geometric DMs (GDMs). The PDMs represent curves or surfaces explicitly and allow direct model interaction; however, unable to adapt to topological change and sensitive to user interaction. For GDMs, the curves and surfaces are represented by using level set functions. They can adapt to the topological change, but increase the computational cost greatly.

In PDMs-based BUS image segmentation approaches, the main work was focused on generating good initial tumor boundary. Madabhushi et al. [40] proposed a fully automatic approach for BUS tumor segmentation by initializing PDMs using the boundary points produced in tumor localization step; and the balloon forces were employed in the extern forces. Chang et al. [41] utilized the sticks filter [42] to enhance edge and reduce speckle noise before using the PDMs. Huang et al. [43] proposed an automatic BUS image segmentation approach by using the gradient vector flow (GVF) model [44], and the initial boundary was obtained by using the watershed approach.

In GDMs-based BUS image segmentation approaches, many researches focused on dealing with the weak boundary and inhomogeneity of BUS images. The two main strategies are (1) making the stopping function independent of image gradient, and (2) applying local statistics to define the speed function. Gomez et al. [45] proposed a BUS image segmentation approach based on the active contour without edges (ACWE) model [46] which defined the stopping term on Mumford-Shah techniques. The initial contour was a five-pixel radius circle centered at a point in the tumor marked by the user. Daoud et al. [47]



built a two-fold termination criterion based on the signal-to-noise ratio and local intensity value. Gao et al. [48] proposed a level set approach based on the method in [49] by redefining the edge-based stop function using phase congruency [50] which was invariant to intensity magnitude, and integrated the GVF model into the level set framework. Liu et al. [80] proposed a GDMs-based approach which enforced priors of intensity distribution by calculating the probability density difference between the observed intensity distributions and the estimated Rayleigh distribution.

Graph-based approaches: graph-based approaches gain popularity in BUS image segmentation because of their flexibility and efficient energy-optimization. The Markov random field - Maximum a posteriori - Iterated Conditional Mode (MRF-MAP-ICM) and the Graph cuts are the two major frameworks in graph-based approaches. MRF-MAP-ICM can model multiple-object segmentation problem and is popular in early BUS image segmentation; Graph cuts models image bi-partition problem and provides an efficient way for MRF energy global optimization. The key issues of applying the two frameworks in BUS image segmentation are the likelihood and prior energies definition and parameters estimation.

MRF-MAP-ICM: Boukerroui et al. [51] stated that healthy and pathological breast tissues presented different textures on BUS images, and proposed to improve the method in [52] by modeling both intensity and texture distributions in the likelihood energy; they also assumed that the texture features represented by using co-occurrence matrix follow the Gaussian distribution; and the parameters were estimated in a way similar to the one in [52]. In [53], the Gaussian parameters in the likelihood energy were defined globally and

specified manually. [54] proposed a one-click user interaction to estimate Gaussian parameters automatically. The user specified a pixel in the tumor and the method opened a small window and a large window to obtain the lesion and background information, respectively. The foreground and background parameters were estimated using the intensity distributions in the small and large windows.

Graph cuts: Xian et al. [38] proposed a fully automatic BUS image segmentation framework in which the graph cuts energy modeled the information from both the frequency and space domains. The data term (likelihood energy) modeled the tumor pose, position and intensity distribution. [55] built the graph on image regions, and initialized it by specifying a group of tumor regions (F) and a group of background regions (B). The weight of any t-link was set to  $\infty$  if the node belonged to  $F \cap B$ , and all the other weights of t-links were set to 0; and the region intensity difference and edge strength discussed in [56] were applied to define the weight function of the smoothness term (prior energy). [55] proposed a discriminative graph cut approach in which the data term was determined online by a pre-trained Probabilistic Boosting Tree (PBT) [57] classifier.

In [58], hierarchical multiscale superpixel classification framework was proposed to define the data term. The hierarchical classifier had four layers (20, 50, 200, and 800 superpixels/nodes) built by using the normalized cut and k-means for multiscale representation; the histogram difference (Euclidean distance) between adjacent superpixels was used to define the weights in the smoothness term. Low optimization speed and locally optimal solution are the two main drawbacks of the MRF-MAP-ICM; while the “shrinking” problem is the main disadvantage of Graph cuts-based approaches.

Learning based approaches: both supervised and unsupervised learning approaches

have been applied to solve the BUS image segmentation problem. Unsupervised approaches are simple and fast, and commonly applied as a preprocessing step to generate candidate image regions. Supervised approaches are good in integrating features at different levels, but not good in applying boundary constraints to generate accurate tumor boundary.

Clustering: Xu et al. [59] proposed a BUS image segmentation method applying the spatial FCM (sFCM) [60] to the local texture and intensity features. In sFCM, the membership value of each point was updated by using its neighbors' membership values. In [59], the number of clusters was set as 2, and the membership values were assigned by using the modes of image histogram as the initial cluster centers. In [61], FCM was applied to pixel intensities for generating image regions in four clusters; then morphology, location and size features were measured for each region; a linear regression model trained on the features was employed to produce the tumor likelihoods for all regions, and the region with the highest likelihood was considered as a tumor. Moon et al. [76] applied FCM to image regions produced by using the mean shift method; the number of clusters was set to 4, and the regions belonging to the darkest cluster were extracted as the tumor candidates. Shan et al. [79] extended the FCM and proposed the neutrosophic l-means (NLM) clustering to deal with the weak boundary problem in BUS image segmentation; and it took the indeterminacy of membership into consideration.

SVM and NN: Liu et al. [62] trained a SVM classifier using local image features to classify small image lattices ( $16 \times 16$ ) into the tumor or non-tumor classes; the radius basis function (RBF) was utilized; and 18 features, including 16 features from co-occurrence matrix and the mean and variance of the intensities, were extracted from a lattice. Jiang et

al. [77] trained Adaboost classifier using 24 Haar-like features [63] to generate a set of candidate tumor regions and trained SVM to determine the false positive and true positive regions. [64] proposed an NN-based method to segment 3D BUS images by processing 2D images slices using local image features. Othman et al. [65] trained two ANNs to determine the best-possible threshold. The two ANNs had 3 layers, 60 nodes in hidden layer, one node in the output layer. The first ANN used the Scale Invariant Feature Transform (SIFT) descriptors as the inputs; and the second employed the texture features from the Grey Level Co-occurrence Matrix (GLCM) as the inputs. [78] trained an ANN to conduct pixel-level classification by using the joint probability of intensity and texture [40] and two new features: the phase in the max-energy orientation (PMO) and radial distance (RD). The NN had 6 hidden nodes and 1 output node.

Deep Learning-based approaches have been reported to achieve state-of-the-art performance for many medical tasks such as prostate segmentation [66], cell tracking [67], muscle perimysium segmentation [68], brain tissue segmentation [69], breast tumor diagnosis [70], etc. However, there is no deep learning-based approach for BUS image segmentation yet. Deep learning models have great potential to achieve good performance because of their ability to characterize big image variations and to learn compact image representation using sufficiently large BUS image dataset. Deep learning architectures based on convolutional neural networks (CNNs) and recurrent neural networks (RNNs) are quite popular in medical image segmentation [66 - 70].

Classical approaches: Three most popular classical approaches were applied to BUS image segmentation: thresholding, region growing and watershed. In BUS image segmentation, thresholding was often used as a pre-segmentation step for tumor localization.

Three main approaches exist in BUS segmentation for selecting the threshold: (1) choose the empirical value as threshold for the entire dataset [71]; (2) select threshold for each image based on domain related rules [40, 78]; and (3) generate threshold automatically based on statistical-decision theory [38, 11]. Region growing extracts image regions by starting from a set of pixels (called seeds) and growing seeds to large regions based on predefined growth criteria. In [78], Shan et al. proposed an automatic seed generation approach. Thresholding was used to generate a group of candidate regions first; and then region ranking criteria based on region location, size and local feature were utilized to determine a true tumor region; and a pixel in the region was selected as the seed. In [72], Kwak et al. defined the cost of growing a region by modelling common contour smoothness and region similarity (mean intensity and size). Watershed could produce more stable results than thresholding and region growing approaches, and selecting the marker(s) is the key issue in watershed segmentation. The first solution is to choose the local minimum gradient as the marker, and further step such as region merging should be involved to avoid over-segmentation. Another solution is to select makers based on predefined criteria that can utilize the task-related priors. Huang et al. [60] selected the markers based on grey level and connectivity. [74] applied watershed to determine the boundaries on binary image. The markers were set as the connected dark regions on the binary image. [75] applied watershed and post-refinement based on grey level and location to generate candidate tumor regions.

There are two major challenges in BUS image segmentation: (1) most BUS image segmentation approaches work well on BUS images collected in controlled settings such

as high image contrast, less artifacts, etc. However, because these approaches heavily depend on non-robust information such as the appearance models of tumor or background tissues, their performance degrades greatly with BUS images having large variations in image quality and degree and location of artifacts; and (2) all previous approaches were evaluated by using private datasets and different quantitative metrics, which make the objective and effective comparisons among the methods impossible. Therefore, it remains challenging to determine the best performance of the breast tumor segmentation algorithms available today, what segmentation strategies are valuable in clinic practice and study, and what image features are helpful and useful in improving segmentation accuracy and robustness.

To overcome the challenges, we are building a BUS benchmark for evaluating segmentation approaches, and the benchmark will be public available soon.

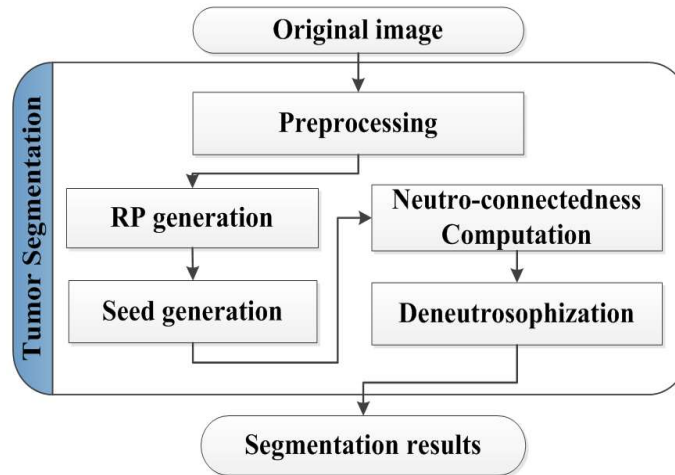


Fig. 5.1. Flowchart of the proposed fully automatic BUS segmentation approach

In this section, we present a fully automatic BUS image segmentation approach based on NC for performing accurate and robust ROI generation, and tumor segmentation.

### 5.3 Overview of The Proposed Approach

In the ROI generation step, the proposed adaptive reference point (RP) generation algorithm can produce the RPs automatically based on the breast anatomy; and the multi-path search algorithm generates the seeds accurately and fast. In the tumor segmentation step, we propose a segmentation framework in which the cost function is defined by using NC map and features from the frequency domain. First, the frequency constraint is built base on the newly proposed edge detector which is invariant to contrast and brightness; and then the tumor pose, position and intensity distribution are modeled to constrain the segmentation in the spatial domain. The well-designed cost function is graph-representable and its global optimum can be found. The flow chart of the proposed approach is shown in Fig. .1.

### 5.4 Preprocessing

The breast tumor reflects lower level of echoes than surrounding tissues, and appears relatively darker (hypoechoic) on BUS image [81]. However, the gray levels, contrast, texture, etc. of B-mode BUS images vary greatly due to the facts that they are operator-dependent and device-dependent. The preprocessing is to normalize intensities and to enhance the hypoechoic regions (candidates of tumor regions). The proposed preprocessing steps are as below:

- 1) Smoothing. A 2-D discrete Gaussian low-pass filter was utilized to smooth the BUS image in the frequency domain (using fast Fourier transform).
- 2) Eliminating the intensity range variability. We applied a linear normalization to align the lower and upper bounds. The linear normalization is defined as below:

$$f_{Lnorm} = \begin{cases} 0, & \text{if } x \leq lbound \\ \frac{(x-lbound) \cdot (Ln-1)}{ubound-lbound}, & \text{if } lbound \leq x \leq ubound \\ Ln-1, & \text{if } x \geq ubound \end{cases} \quad (52)$$

In Eq. (52),  $Ln$  is the number of gray levels;  $lbound$  and  $ubound$  are defined as  $Q(0.05)$  and  $Q(0.95)$ , respectively.  $Q$  is the quantile function on the cumulative distribution of the histogram.

$$Z(x; z_a, z_b, z_c) = \begin{cases} 1, & \text{if } x \leq z_a \\ 1 - \frac{(x-z_a)^2}{(z_c-z_a)(z_b-z_a)}, & \text{if } z_a \leq x \leq z_b \\ \frac{(x-z_c)^2}{(z_c-z_a)(z_c-z_b)}, & \text{if } z_b \leq x \leq z_c \\ 0, & \text{otherwise} \end{cases} \quad (53)$$

3) Enhancing hypoechoic regions. An adaptive Z-shaped function (Eq. (53)) was proposed to reverse the intensities and transform them into  $[0, 1]$ . The shape of the function is determined by the characteristics of image adaptively. In Eq. (53), the parameters,  $z_a$  and  $z_c$ , determine the nonlinear range of the curve; the parameter  $z_b$  is used to adjust the steepness of the curve which should be decided adaptively according to the skewness of the intensity distribution:

$$z_b = \begin{cases} (z_a + z_c)/2, & \text{if } SN \leq 0 \\ [z_a + z_c(1 - SN)]/2, & \text{if } SN > 0 \end{cases} \quad (54)$$

$$SN = \frac{\sqrt{(n-1)(n-2)}}{n} \cdot \frac{1/n \sum_{i=1}^n (x_i - \bar{x})^3}{[1/n \sum_{i=1}^n (x_i - \bar{x})^2]^{3/2}} \quad (55)$$

where  $x_i$  is the intensity of the  $i$ th pixel,  $\bar{x}$  is mean of image intensities,  $n$  is the number of pixels,  $z_c$  is determined by the mean of the intensities, and  $z_a$  is a constant set as 20.  $SN$  is the bias-corrected skewness [82] which measures the asymmetry of the image intensity distribution. The larger the skewness ( $SN$ ) becomes, the more the mass of the distribution concentrates on the left side, which will result a steeper Z-shaped function (small  $z_b$ ).



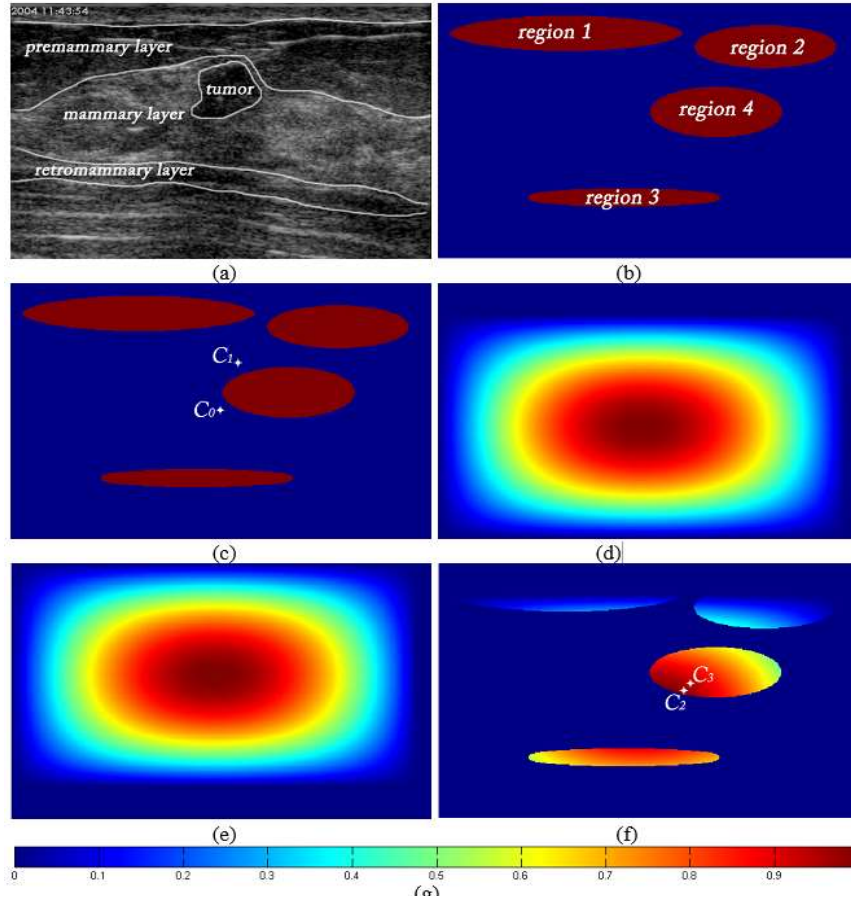


Fig. 5.2. RP generation for a synthetic image. (a) Three major layers of the breast in a BUS image; (b) the result of the BUS image after preprocessing; (c) a synthetic image ( $M = 300$ ,  $N = 500$ ); (d)  $C_0$  and  $C_1$ ; (e)  $w_I$  with  $X_1^L = 1$ ,  $X_1^R = 14$ ,  $Y_1^T = 38$ , and  $Y_1^D =$ ; (f)  $C_2$  and  $C_3$  on the image generated by the third iteration of Algorithm 5.1; (g) the color bar.

### 5.5 Adaptive Reference Point Generation

A reference point (RP) is a position in a BUS image for ranking other pixels or regions. If a pixel is close to the RP, it will have a large probability to be in the lesion. In many fully automatic segmentation methods, the RP was defined as a pixel at the fixed position, which led the failure of these algorithms when the actual tumor location was far away from the predefined RP. In this section, we propose a novel algorithm (Algorithm

5.1) for selecting RP from the preprocessed image automatically and adaptively. The biological foundation for the proposed method is based on [83]: the breast has three major layers from the skin of the breast: the premammary (PM) layer, the mammary layer, and the retromammary (RM) layer (Fig. 5.2(a)); the PM layer lies between the skin and the mammary layer, and contains subcutaneous fat mainly; the mammary layer is in the middle of the three layers, and breast tumors arise in this layer; and the RM layer lies between the mammary layer and the chest wall and contains mainly the fat as well.

Now we propose two definitions for Algorithm 5.1. The first definition is the weighted density center which will move to the tumor regions iteratively. The origin of the image coordinates is at the top-left corner. The *weighted density center* at the  $i$ th iteration is defined

$$C_i = \frac{\sum_{x,y} \left( (x, y) \cdot \prod_{j=0}^{i-1} w_j(x, y) \cdot I'(x, y) \right)}{\sum_{x,y} \left( \prod_{j=1}^{i-1} w_j(x, y) \cdot I'(x, y) \right)}, x = 1, 2, \dots, M, \text{ and } y = 1, 2, \dots, N \quad (56)$$

where  $(x, y)$  are the coordinates of the pixel,  $I'$  is the image after preprocessing,  $w_j$  is the  $j$ th weighting function, and  $M$  and  $N$  are the numbers of rows and columns of the image, respectively. The initial center  $C_0$  is defined as the geometric center of the image and the number of *weighted density centers* will be determined by Algorithm 5.1.

In Eq. (56), without considering the influence of the weighting functions, center  $C_i$  will move to the higher intensity region of  $I'$ . However, the fats in the PM and RM layers also have high intensities in the preprocessed image, which make  $C_i$  diverge from the real tumor region. The weighting function is proposed to solve the above problem based on the fact that these normal regions are mainly from the fats in PM and RM layers, while

the mammary layer lies in their middle. The weighting function is proposed to attenuate the intensities of the surrounding regions and the  $i$ th weighting function is defined as

$$w_i(x, y) = \begin{cases} 0, & \left( x < X_i^L \text{ or } x > N - X_i^R \text{ or } y < Y_i^T \text{ or } y > M - Y_i^D \right) \\ \frac{(x - X_i^L) \cdot (N - X_i^R - x) \cdot (y - Y_i^T) \cdot (M - Y_i^D - y)}{\left[ (N - X_i^L - X_i^R) / 2 \right]^2 \cdot \left[ (M - Y_i^T - Y_i^D) / 2 \right]^2}, & \text{otherwise} \end{cases} \quad (57)$$

where  $X_i^L, X_i^R, Y_i^T$  and  $Y_i^D$  are the distances between the bounds of the  $i$ th weighting function and their corresponding borders (left: 1, right: M, top: 1, and bottom: N) of the image, respectively. The values of  $X_i^L, X_i^R, Y_i^T$  and  $Y_i^D$  are updated according to the weighted density centers iteratively. The initial weight  $w_0$  is a matrix with all elements equal to 1.

---

**Algorithm 5.1: RP generation**

---

Inputs:  $C_0, w_0, I'$

Output: the position of RP:  $RP_0$

---

1. For  $i = 1: N_{MAX}$
  2. Calculate new center  $C_i$  using Eq. (5), and  $RP_0 \leftarrow C_i$ ;
  3. If  $\|C_i - C_{i-1}\| < \varepsilon_I$  then
  4.   break;
  5. Else
  6.   Update the bounds ( $X_i^L, X_i^R, Y_i^T$ , and  $Y_i^D$ ) of the weighting function:
  7.    If  $C_i^X - C_{i-1}^X > 0$  then  $X_i^L = C_i^X - C_{i-1}^X, X_i^R = X_{i-1}^R$
  8.    Else  $X_i^L = X_{i-1}^L, X_i^R = C_{i-1}^X - C_i^X$
  9.    If  $C_i^Y - C_{i-1}^Y > 0$  then  $Y_i^T = C_i^Y - C_{i-1}^Y, Y_i^D = Y_{i-1}^D$
  10.   Else  $Y_i^T = Y_{i-1}^T, Y_i^D = C_{i-1}^Y - C_i^Y$
  11. Update the weighting function  $w_{i+1}$  using Eq. (6);
  12. End
  13. Return  $RP_0$ ;
- 

In Algorithm 5.1, the RP is generated by updating the weighting functions and *weighted density centers* iteratively. The algorithm will stop when it reaches the maximum

number of iterations ( $N_{MAX}$ ) or the Euclidean distance between two adjacent weighted density centers is smaller than a predefined value  $\varepsilon_I$  ( $N_{MAX} = 100$  and  $\varepsilon_I = 2$  in all of the experiments).  $(C_i^X, C_i^Y)$  and  $(C_{i-1}^X, C_{i-1}^Y)$  represent the coordinates of the weighted density centers at the  $i$ th and the  $(i-1)$ th iterations, respectively. In order to explain the procedure of Algorithm 5.1 clearly, we applied the algorithm to generate RP of a synthetic image (Fig. 5.2); and the RP generation results of real B-mode BUS images are shown in Fig. 5.3.

In Fig. 5.2(b), regions 1 - 3 are used to simulate the fat regions around the mammary layer (middle layer); region 4 is the tumor in the mammary layer. Because the four regions are distributed mainly in the top right part of the image, the weighted density center  $C_I$  moves to the upper right of  $C_0$  (Fig. 5.2(c)). As shown in Fig. 5.2(d) and Fig. 5.2(e), the weighting function  $w_I$  is applied to correct the deviation by moving the center of the weighting function to the lower left. Fig. 5.2(f) shows that the intensities of the three regions (regions 1-3) around the target (region 4) are attenuated after the third iteration, and  $C_2$  and  $C_3$  are already in the target region.

---

**Algorithm 5.2: Seed generation**


---

Inputs :  $RP_0, I$

Outputs : *seed*

---

1. Extend a  $RP_0$  to  $N_{rp}$  RPs;
  2. Initialize an array  $c$  with size  $N_{rp}$  to save the candidate positions;
  3. For  $i = 1 : N_{rp}$
  4.   Initialize the start position  $p$  to be  $RP_i$ ;
  5.   Iterate until converge to a candidate position  $c[i]$ :
  6.     Calculate next position  $next(p)$  using Eq. (9);
  7.     If  $\|next(p) - p\| < \varepsilon_2$  then  $c[i] \leftarrow p$ ; break current iteration;
  8.     Else  $p \leftarrow next(p)$ ;
  9.   End
  10. Choose the point in  $c$  with the maximum local mean (using Eq. (12)) as our final seed;
-

### 5.6 Seed Generation

In this section, we will use the RP as the initial point to search the seed. We develop a multipath search algorithm to obtain the seed in the tumor. The advantages of the proposed algorithm are: (1) the seed is generated iteratively based on the local mean of intensities rather than heavily depended on the distances between the RP and the candidate regions [40, 84], which will be more accurate than the existing methods (refer Fig. 5.3), and (2) it generates the seed with high speed (refer Table 5.1).

In Algorithm 5.2,  $RP_0$  is the position of the final reference point and  $I'$  is the pre-processed image. We extend the reference point into multiple points. The reference point's position along the  $i$ th direction is defined as

$$RP_i = RP_0 + [h \cdot (\cos\theta_i, \sin\theta_i)], \quad i = 1, 2, \dots, n_{dre} \quad (58)$$

$$\theta_i = 2\pi(i - 1)/n_{dre} \quad (59)$$

where  $n_{dre}$  is the number of directions,  $\theta_i$  denotes the angle of the  $i$ th direction relative to  $RP_0$ , and  $h$  is the step size (12 pixels) determined by experiments.

Mean shift [84, 85] is utilized to calculate the next position of the current point (Eq. (60)). We shift position  $p$  to a new position  $next(p)$  when the distance between  $next(p)$  and  $p$  is larger than a predefined value ( $\varepsilon_2$ ), and  $next(p)$  is defined by [85]

$$next(p) = \frac{\sum_{i=1}^n K_H(p_i - p) \cdot I'(p_i) \cdot p_i}{\sum_{i=1}^n K_H(p_i - p) \cdot I'(p_i)} \quad (60)$$

where  $I'$  is the normalized image,  $p_i$  is the coordinate of the  $i$ th point of  $I'$ , and  $K_H$  is a kernel function defined by

$$K_H(p_i - p) = F[H^{(-1/2)} \times (p_i - p)] \quad (61)$$

where  $H$  is a bandwidth matrix,  $H = \text{diag}(h^2, h^2)$  and  $F$  is the *unit flat kernel* [84] centered at position  $p$ . After the iterations on each RP, we obtain  $N_{rp}$  candidate seeds. The one with the maximum local sum of intensities will be the final seed

$$seed = \underset{p}{\operatorname{argmax}} (M(p)), p \in \{c[i] | i = 1, 2, \dots, N_{rp}\} \quad (62)$$

$$M(p) = \sum_{i=1}^n K_H(p_i - p) \cdot I(p_i) \quad (63)$$

where  $M(p)$  is the local mean of the candidate seed  $p$ . The predefined value  $\varepsilon_2 = 2$  determined by experiments.

#### 5.7 NC Computation and Deneutrosophication

In order to apply the proposed *NC* to model the uncertainty and indeterminacy of tumor segmentation problem, the specific forms of  $\mu_T$  and  $\mu_C$  need to be defined. Let  $z_j$  and  $z_k$  be two 8-connected neighbors. We define  $\mu_T$  as the same as fuzzy *spel* affinity in [7].

$$\begin{aligned} \mu_T(z_j, z_k) &= w_1 h_1(z_j, z_k) + w_2 h_2(z_j, z_k) \\ h_1(z_j, z_k) &= \exp \left( -1/2 \left[ \frac{(W(z_j) + W(z_k)) - m_1}{s_1} \right]^2 \right) \\ h_w(z_j, z_k) &= \exp \left( -1/2 \left[ (|W(z_j) - W(z_k)| - m_2)/s_2 \right]^2 \right) \end{aligned} \quad (64)$$

In Eq. (64),  $W(z)$ , is the value of pixel in the normalized image; function  $h_1$  computes the degree of difference in appearance between the two adjacent pixels and the object of interest; function  $h_2$  is used to impose the boundary constraint;  $m_1$  and  $s_1$  are the mean and standard deviation of the gray values ( $W$ ) in the object of interest, respectively;  $m_2$  and

$s_2$  are the mean and standard deviation of gray gradient values in the object of interest, respectively.

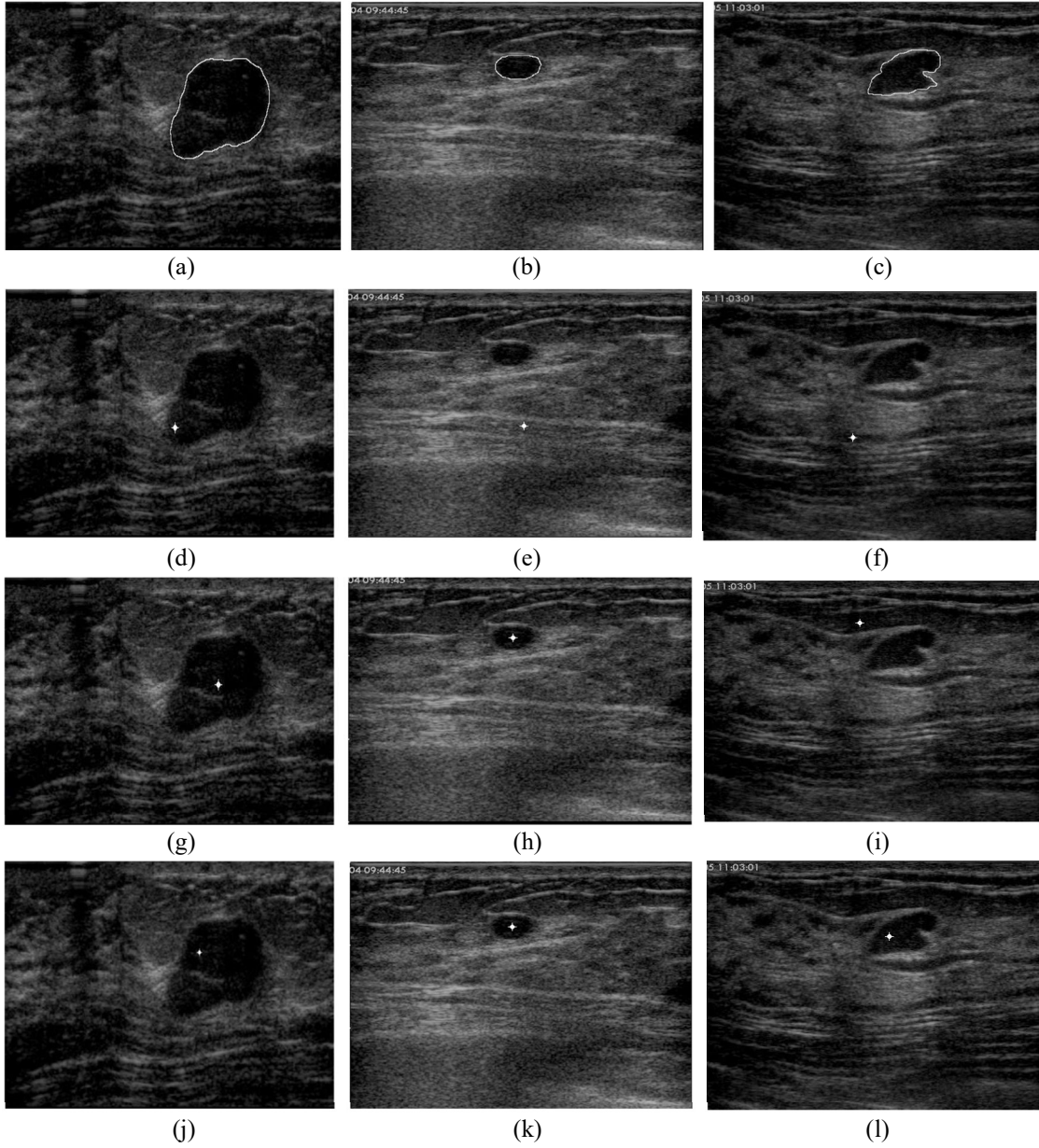


Fig. 5.3. The seed generation of four BUS images: (a) – (c) the original images with delineation by an experienced radiologist; (d) – (f) the seeds generated by the method in [40]; (g) – (i) the seeds generated by the method in [15]; and (j) – (l) the seeds generated by the proposed method.

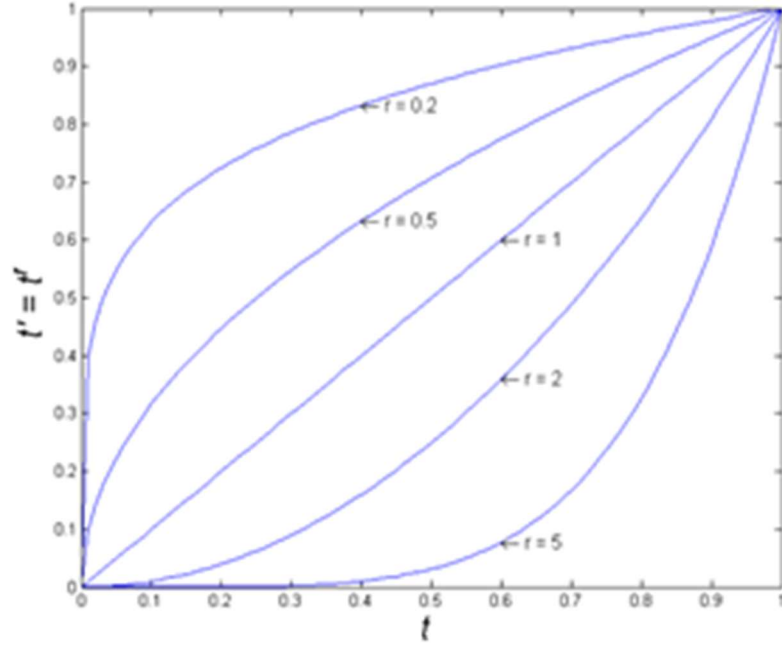


Fig. 5.4. Domain reduction functions.

The confidence of connectedness between two adjacent points is defined as

$$\mu_C(z_j, z_k) = \max \left( \exp \left( -1/2 \left[ \frac{(W(z_j) - m_{12})}{s_{12}} \right]^2 \right), \exp \left( -1/2 \left[ \frac{(W(z_k) - m_{12})}{s_{12}} \right]^2 \right) \right), \quad (65)$$

where  $m_{12}$  and  $s_{12}$  define a plane between the intensity distributions of object of interest (tumor region) and the non-object (normal tissues). The confidence of connectedness between  $z_j$  and  $z_k$  will decrease when  $W(z_j)$  or  $W(z_k)$  is close to  $m_{12}$ . For any pair of nonadjacent pixels,  $\mu_T$  is set to 0 and  $\mu_C$  is 1.

We define *deneutrosophication* to represent the decision-making process. In this section, we describe a common strategy used for *deneutrosophication*. At a high level, the proposed *deneutrosophication* involves two steps to perform the tumor segmentation:

- Domain reduction. The two domains of NC will be reduced into one domains ( $t'$ ).



- Graph cuts segmentation.  $t'$  will be applied to constrain the graph cuts to perform the final segmentation.

As shown in Fig. 5.4, a group of power functions will be employed to do the domain reduction;  $r$  is defined as

$$r = \begin{cases} i(p, q), & \text{if } i(p, q) < 0.5 \\ 1 / i(p, q), & \text{if } i(p, q) \geq 0.5 \end{cases} \quad (66)$$

where  $i(p, q)$  is  $1 - C(p, q)$ . The domain reduction will decrease the connectedness between pixels if the corresponding indeterminacy is bigger than 0.5; otherwise, the connectedness will increase. The  $f'$  is set to  $1 - t'$ .

Graph cuts is chosen to perform the second step of *de-neutrosophication*, and the main reason is that it is easy to integrate different constraints from multi-domains into the segmentation framework in a soft manner. The  $t'$  and  $f'$  will be used to constrain the global term (data term) of the graph cuts; therefore, the final segmentation will not only consider the local differences and global similarity, but also try to segment the pixels with high connectedness in the same classes (tumor or normal tissues).

If function  $\mu_C$  is identically equal to 1 ( $i(p, q) = 0$ ), NC will degenerate into the fuzzy connectedness in Ref. [7].

## 5.8 Experimental Results

### 5.8.1 Dataset, Parameters, and Metrics

The proposed method was evaluated on a B-mode BUS image database with 131 cases (60 benign and 71 malignant). The radiologist's manually delineated boundaries were used as the golden standards and our segmentation results were evaluated by comparing

with them.

The area error metrics and boundary error metrics were employed to evaluate the performance of the proposed segmentation method. The area error metrics include the Dice's coefficient ( $DSC$ ) and false positive ratio ( $FPR$ ).

$$DSC = \frac{|A_m \cap A_r|}{|A_m \cup A_r|}$$

$$FPR = \frac{|A_m \cup A_r - A_m|}{|A_m|}$$

where  $A_m$  is the pixel set of the tumor region manually outlined by the radiologist, and  $A_r$  is the pixel set of the tumor region generated by the proposed method. The average Hausdorff error (AHE) is used to assess the average performance of boundaries.

The weight  $w_l$  was set to 0.5[12]. The parameters of prior distribution  $(m_l, s_l)$ ,  $(m_2, s_2)$  and  $(m_{l2}, s_{l2})$  were select as (0.13, 0.2), (0.62, 0.07) and (0.38, 0.2) by experiments, respectively.

### 5.8.2 Results

The ROIs are generated automatically from the original BUS images, and the seed regions are small square (side lengths = 21 pixels) regions around the seed points. Figs. 5.5(a) and (d) are two ROIs generated automatically from the original BUS images. As shown in Figs. 5.5(b) and (e), the fuzzy connectedness leaks through the weak parts (red circles) of the boundaries, and links the tumor region with the nearby normal regions. It will produce wrong segmentation results (high false positives). Figs. 5.5(c) and (f) show the confidence of connectedness calculated by using the proposed method.

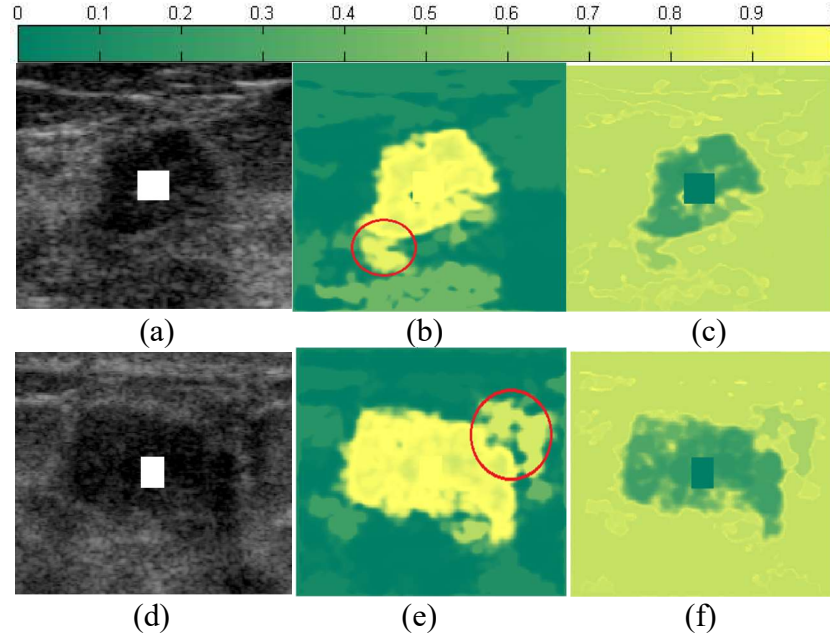


Fig. 5.5. Calculating connectedness of two BUS images: (a) and (d) two ROIs (rectangle) of the original BUS images with weak boundaries, and the white squares are seed regions; (b) and (e) the strength of fuzzy connectedness between each pixel and the seed regions; (c) and (f) the inverse map of the confidence of connectedness ( $1 - C$ ).

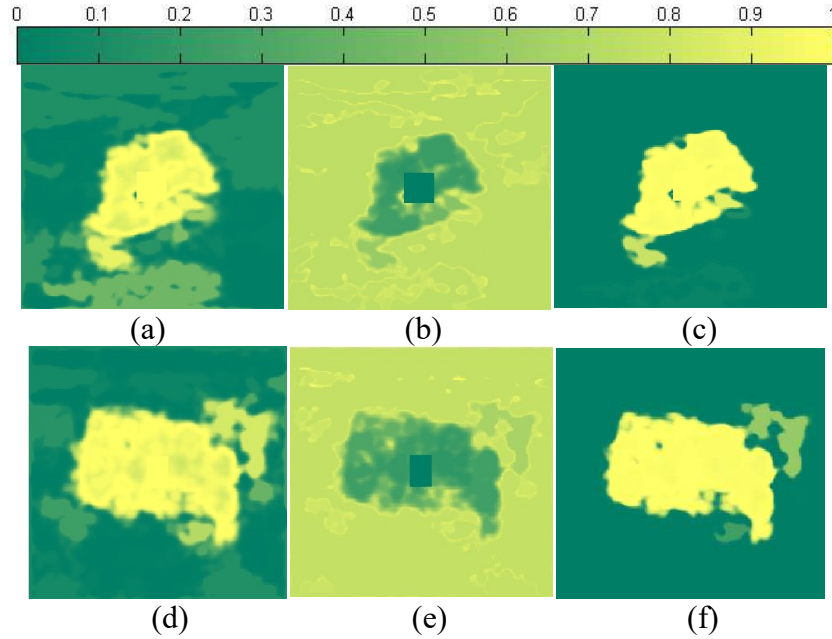


Fig. 5.6 Deneutrosophication: (a) and (d) the fuzzy connectedness of two BUS images; (b) and (e) the inverse map of confidence of connectedness; (c) and (f) the results of domain reduction ( $t'$ ).

The normal regions with high fuzzy connectedness in Fig. 5.5(b) and (e) have relatively low confidence values in Figs. 5.5(c) and (f). It will prevent the leakage of the fuzzy connectedness.

In order to apply the NC to solve the tumor segmentation problem, we reduced the three domains ( $t$ ,  $i$  and  $f$ ) into two domains ( $t'$  and  $f'$ ) using the proposed method. As shown in Fig. 5.6, the strength of the connectedness between the tumor-like region and tumor is reduced by applying the indeterminacy of connectedness.

Based on the same database, we compared our method with the fuzzy connectedness based segmentation method. The tumor segmentation of three ROIs of BUS images are shown Fig 5.7. Figs. 5.7(a) – (r) show the intermediated results and the final results of the fuzzy connectedness method and the proposed neutro-connectedness method. As shown in Figs. 5.7(c), (i) and (o), the fuzzy connectedness leaks through the weak boundaries and links the tumor regions with the nearby normal regions, which finally results in the increasing of the false positive (Figs 5.7. (e), (k) and (g)). Fig. 5.7 (d), (j) and (p) shows that the false connectedness produced by the fuzzy connectedness can be largely reduced by applying the proposed neutro-connectedness method, and the results of the proposed method is much better than that of the fuzzy connectedness method.

To validate the overall performance of the proposed method, the SIR, FPR and AHE were computed and showed in Table 5.1. As shown in Table 5.1, the SIR of the proposed method on both the benign and the malignant cases are higher than the SIR of fuzzy connectedness method; which indicates that the results of the proposed segmentation method is more similar to the true tumor region than that of the fuzzy connectedness method.

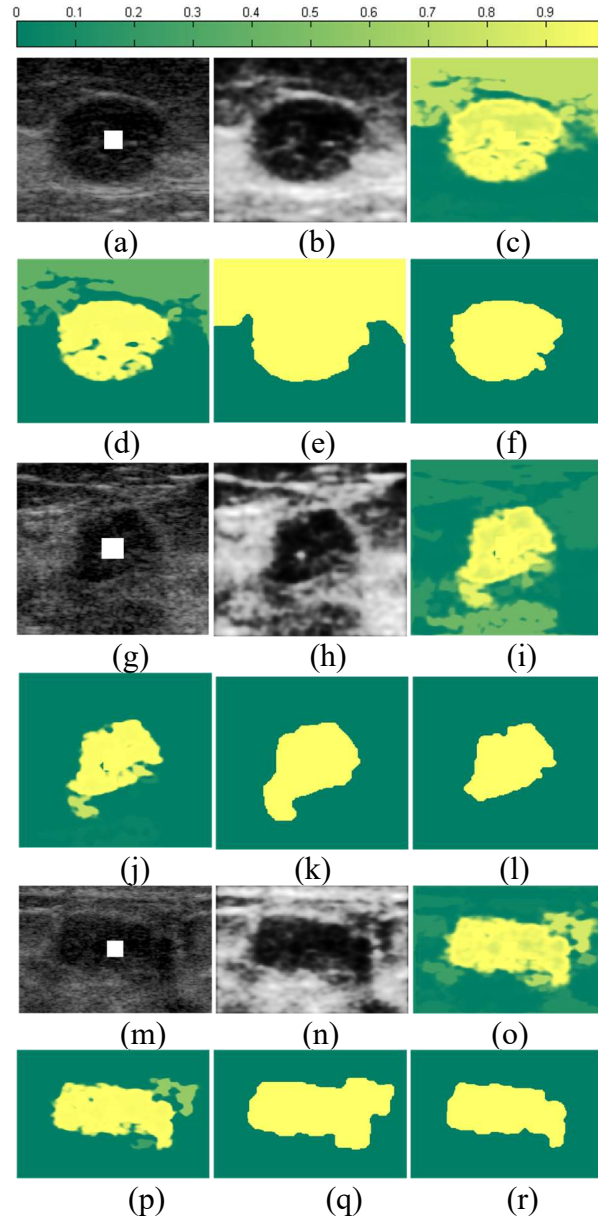


Fig. 5.7. BUS image segmentation: (a), (g) and (m) three ROIs with seed regions (white rectangle); (b), (h) and (n) the results of the preprocessing step; (c), (i) and (o) the results of fuzzy connectedness; (d), (j) and (p) the confidence of connectedness ( $1-C$ ); (e), (k) and (q) the results of the fuzzy connectedness based segmentation; (f), (l) and (r) the results of the proposed method.

The FPR of the proposed method is much smaller than the FPR of the fuzzy connectedness method; therefore, the proposed method can exclude most of the tumor-like re-

gions (shadows and fat) out of the tumor region by employing the neutro-connectedness. Our smaller AHE also shows that the tumor boundaries produced by the proposed method is closer to the true tumor boundaries than boundaries produced by the fuzzy connectedness method.

Table 5.1. Average Performance of Tumor Segmentation Approaches.

| Cases |     | Fuzzy connectedness based segmentation |                |            | Proposed method |                |            |
|-------|-----|--|----------------|------------|-----------------|----------------|------------|
|       |     | <i>DSC</i> (%)                         | <i>FPR</i> (%) | <i>AHE</i> | <i>DSC</i> (%)  | <i>FPR</i> (%) | <i>AHE</i> |
| A     | 60  | 79.47                                  | 22.30          | 20.0       | 80.92           | 6.90           | 18.0       |
| B     | 71  | 78.48                                  | 23.99          | 24.0       | 82.43           | 4.99           | 21.6       |
| C     | 131 | 78.93                                  | 22.74          | 22.2       | 79.65           | 9.85           | 20.9       |

A: benign tumors; B: malignant tumors; C: total.

## CHAPTER 6

### CONCLUSION AND FUTURE WORK

This dissertation is comprised of my main work in Neutro-Connectedness (NC) theory, algorithms and applications. The main contributions are summarized as follows.

(1) The proposed NC theory generalizes the traditional concept of connectedness, and has one additional domain, the confidence of connectedness, to model “hidden factors”. With the additional domain, NC can deal with more complex problems, e.g., low quality image segmentation and noisy data analysis.

(2) A general algorithm for NC computation is also given in section 2.3 the proposed algorithm calculates the degrees of connectedness and the confidence of connectedness simultaneously and can uncovers the topological structure of a dataset by using the output NC forest.

(3) The proposed NC-Cut is a hybrid interactive segmentation method that needs much less user interaction than seed-based methods, and is less sensitive to the initial ROI than state-of-the-art ROI-based methods. We formulate NC-Cut using both pixel-wise appearance models and region-based NC, which can overcome the two problems of initial ROI-dependence and intense user interactions in interactive image segmentation approaches.

(4) The proposed effective interactive segmentation (EISeg) method reduces the degree of arbitrariness of user interaction in interactive image segmentation greatly, and needs much less user interaction than state-of-the-art ROI-based methods. EISeg provides user with objective visual clues of topological property by computing the boundary connectedness map and forest, and gives user three sample interaction protocols to guide user

interaction according to the visual clues. The experiments demonstrate that the proposed EISeg method guides interaction effectively, and achieves better results with much less user interaction than state-of-the-art approaches.

(5) A fully automatic breast tumor detection approach is proposed by modeling tumor structure using NC. The proposed methods are based on solid biologic foundations from breast anatomy and can generate the RPs adaptively and accurately; and the approach models the spatial topological property of image pixels using the neutro-connect-  
edness to handle the weak boundary problem of BUS images.

In the future, I will focus on improving the NC computation algorithm in terms of scalability, robustness and low time cost; we will also explore the possibility of applying NC to data clustering, topological data analysis, saliency detection, unsupervised image segmentation, object tracking, etc.



## REFERENCES

- [1] T. Opsahl, and P. Panzarasa, "Clustering in weighted networks," *Social Networks*, vol. 31, no. 2, pp. 155-163, 2009/05/01/, 2009.
- [2] D. J. Watts, and S. H. Strogatz, "Collective dynamics of 'small-world' networks," *Nature*, vol. 393, no. 6684, pp. 440-442, 1998.
- [3] L. Chen, "Topological structure in visual perception," *Science*, 1982.
- [4] R. Casati, "Topology and cognition," *Encyclopedia of cognitive science*, 2000.
- [5] A. Rosenfeld, "Fuzzy digital topology," *Information and Control*, vol. 40, no. 1, pp. 76-87, 1979.
- [6] L. Chen, H. D. Cheng, and J. P. Zhang, "Fuzzy Subfiber and Its Application to Seismic Lithology Classification," *Inf. Sci. Applications*, vol. 1, no. 2, pp. 77-95, Mar, 1994.
- [7] J. K. Udupa, and S. Samarasekera, "Fuzzy connectedness and object definition: Theory, algorithms, and applications in image segmentation," *Graph. Models*, vol. 58, no. 3, pp. 246-261, May, 1996.
- [8] J. K. Udupa, P. K. Saha, and R. A. Lotufo, "Relative fuzzy connectedness and object definition: Theory, algorithms, and applications in image segmentation," *IEEE Trans. Pattern Anal. Mach. Intell.*, vol. 24, no. 11, pp. 1485-1500, Nov, 2002.
- [9] H. He, and Y. Q. Chen, "Fuzzy aggregated connectedness for image segmentation," *Pattern Recognit.*, vol. 34, no. 12, pp. 2565-2568, Dec, 2001.
- [10] K. C. Ciesielski, P. A. Miranda, A. X. Falcão et al., "Joint graph cut and relative fuzzy connectedness image segmentation algorithm," *Med. Image Anal.*, vol. 17, no. 8, pp. 1046-1057, 2013.
- [11] M. Xian, H. D. Cheng, and Y. Zhang, "A Fully Automatic Breast Ultrasound Image Segmentation Approach Based on Neutro-Connectedness," in *Proc. ICPR*, 2014, pp. 2495-2500.
- [12] Y. Boykov, and M. P. Jolly, "Interactive graph cuts for optimal boundary & region segmentation of objects in ND images," in *Proc. IEEE ICCV*, 2001, pp. 105-112.
- [13] S. Vicente, V. Kolmogorov, and C. Rother, "Graph cut based image segmentation with connectivity priors," in *Proc. IEEE CVPR*, 2008, pp. 1-8.
- [14] J. Stuhmer, P. Schroder, and D. Cremers, "Tree Shape Priors with Connectivity Constraints using Convex Relaxation on General Graphs," in *Proc. IEEE ICCV*, 2013, pp. 2336-2343.

- [15] J. Shan, H. D. Cheng, and Y. X. Wang, "A novel automatic seed point selection algorithm for breast ultrasound images," in Proc. ICPR, 2008, pp. 3990-3993.
- [16] M. Xian, Y. Zhang, H.-D. Cheng et al., "Neutro-connectedness cut," IEEE Trans. Image Process., vol. 25, no. 10, pp. 4691-4703, 2016.
- [17] A. K. Sinop, and L. Grady, "A Seeded Image Segmentation Framework Unifying Graph Cuts And Random Walker Which Yields A New Algorithm," in Proc. IEEE ICCV, 2007, pp. 1-8.
- [18] K. C. Ciesielski, P. A. Miranda, A. X. Falcão et al., "Joint graph cut and relative fuzzy connectedness image segmentation algorithm," Med. Image Anal., vol. 17, no. 8, pp. 1046-1057, 2013.
- [19] A. X. Falcão, J. K. Udupa, S. Samarasekera et al., "User-steered image segmentation paradigms: Live wire and live lane," Graph. Models, vol. 60, no. 4, pp. 233-260, 1998.
- [20] E. N. Mortensen, and W. A. Barrett, "Interactive segmentation with intelligent scissors," Graph. Models, vol. 60, no. 5, pp. 349-384, 1998.
- [21] S. Xiang, F. Nie, and C. Zhang, "Interactive natural image segmentation via spline regression," IEEE Trans. Image Process., vol. 18, no. 7, pp. 1623-32, Jul, 2009.
- [22] T. V. Spina, P. A. de Miranda, and A. X. Falcao, "Hybrid approaches for interactive image segmentation using the live markers paradigm," IEEE Trans. Image Process., vol. 23, no. 12, pp. 5756-69, Dec, 2014.
- [23] A. X. Falcao, J. K. Udupa, and F. K. Miyazawa, "An ultra-fast user-steered image segmentation paradigm: live wire on the fly," IEEE Trans. Med. Imaging, vol. 19, no. 1, pp. 55-62, Jan, 2000.
- [24] P. A. Miranda, A. X. Falcao, and T. V. Spina, "Riverbed: a novel user-steered image segmentation method based on optimum boundary tracking," IEEE Trans. Image Process., vol. 21, no. 6, pp. 3042-52, Jun, 2012.
- [25] A. X. Falcao, J. Stolfi, and R. de Alencar Lotufo, "The image foresting transform: theory, algorithms, and applications," IEEE Trans. Pattern Anal. Mach. Intell., vol. 26, no. 1, pp. 19-29, Jan, 2004.
- [26] C. Rother, V. Kolmogorov, and A. Blake, "Grabcut: Interactive foreground extraction using iterated graph cuts," ACM Trans. Graph., vol. 23, pp. 309-314, 2004.
- [27] V. Lempitsky, P. Kohli, C. Rother et al., "Image segmentation with a bounding box prior," in Proc. IEEE ICCV, 2009, pp. 277-284.

- [28] M. Tang, L. Gorelick, O. Veksler et al., "GrabCut in One Cut," in Proc. IEEE ICCV, 2013, pp. 1769-1776.
- [29] S. Han, W. Tao, D. Wang et al., "Image segmentation based on GrabCut framework integrating multiscale nonlinear structure tensor," IEEE Trans. Image Process., vol. 18, no. 10, pp. 2289-302, Oct, 2009.
- [30] J. Wu, Y. Zhao, J.-Y. Zhu et al., "Milcut: A sweeping line multiple instance learning paradigm for interactive image segmentation," in Proc. IEEE CVPR, 2014, pp. 256-263.
- [31] M. Tang, I. B. Ayed, and Y. Boykov, "Pseudo-Bound Optimization for Binary Energies," in Proc. IEEE ECCV, pp. 691-707: Springer, 2014.
- [32] S.D. Jain, K. Grauman, "Predicting Sufficient Annotation Strength for Interactive Foreground Segmentation", in Proc. IEEE ICCV, 2013, pp. 1313-1320.
- [33] P. Scheunders, "A multivalued image wavelet representation based on multiscale fundamental forms," IEEE Trans. Image Process., vol. 11, no. 5, pp. 568-75, 2002.
- [34] R. Achanta, A. Shaji, K. Smith et al., "SLIC superpixels compared to state-of-the-art superpixel methods," IEEE Trans. Pattern Anal. Mach. Intell., vol. 34, no. 11, pp. 2274-2282, 2012.
- [35] D. Martin, C. Fowlkes, D. Tal et al., "A database of human segmented natural images and its application to evaluating segmentation algorithms and measuring ecological statistics," in Proc. IEEE ICCV, 2001, pp. 416-423.
- [36] T. Liu, Z. Yuan, J. Sun et al., "Learning to detect a salient object," IEEE Trans. Pattern Anal. Mach. Intell., vol. 33, no. 2, pp. 353-367, 2011.
- [37] R. L. Siegel, K. D. Miller, and A. Jemal, "Cancer statistics, 2015," CA-Cancer J. Clin., vol. 65, no. 1, pp. 5-29, 2015.
- [38] M. Xian, Y. Zhang, and H. D. Cheng, "Fully automatic segmentation of breast ultrasound images based on breast characteristics in space and frequency domains," Pattern Recognit., vol. 48, no. 2, pp. 485-497, 2015.
- [39] M. Xian, F. Xu, H. D. Cheng *et al.*, "EISeg: Effective interactive segmentation," in Proc. ICPR, 2016, pp. 1982-1987.
- [40] A. Madabhushi, and D. N. Metaxas, "Combining low-, high-level and empirical domain knowledge for automated segmentation of ultrasonic breast lesions," IEEE Trans. Med. Imaging, vol. 22, no. 2, pp. 155-169, Feb, 2003.

- [41] R.-F. Chang, W.-J. Wu, W. K. Moon et al., "Segmentation of breast tumor in three-dimensional ultrasound images using three-dimensional discrete active contour model," *Ultrasound in medicine & biology*, vol. 29, no. 11, pp. 1571-1581, 2003.
- [42] R. N. Czerwinski, D. L. Jones, and W. D. O'Brien Jr, "Detection of lines and boundaries in speckle images-application to medical ultrasound," *IEEE Trans. Med. Imaging*, vol. 18, no. 2, pp. 126-136, 1999.
- [43] Y.-L. Huang, and D.-R. Chen, "Automatic contouring for breast tumors in 2-D sonography.", in *Proc. IEEE EMBS*, 2006, pp. 3225-3228.
- [44] C. Xu, and J. L. Prince, "Generalized gradient vector flow external forces for active contours," *Signal Processing*, vol. 71, no. 2, pp. 131-139, 1998.
- [45] W. Gómez, A. Infantosi, L. Leija, W. Pereira, Active Contours without Edges Applied to Breast Lesions on Ultrasound, in *Proc. Springer MEDICON*, 2010, pp. 292-295.
- [46] T. F. Chan, and L. A. Vese, "Active contours without edges," *IEEE Trans. Image Process.*, vol. 10, no. 2, pp. 266-277, Feb, 2001.
- [47] M. I. Daoud, M. M. Baba, F. Awwad et al., "Accurate Segmentation of Breast Tumors in Ultrasound Images Using a Custom-Made Active Contour Model and Signal-to-Noise Ratio Variations." in *Proc. IEEE SITIS*, pp. 137-141.
- [48] L. Gao, X. Liu, and W. Chen, "Phase-and gvf-based level set segmentation of ultrasonic breast tumors," *Journal of Applied Mathematics*, vol. 2012, pp. 1-22, 2012.
- [49] C. Li, C. Xu, C. Gui et al., "Distance regularized level set evolution and its application to image segmentation," *IEEE Trans. Image Process.*, vol. 19, no. 12, pp. 3243-3254, 2010.
- [50] P. Kovesei, "Phase congruency: A low-level image invariant," *Psychological Research*, vol. 64, no. 2, pp. 136-148, 2000/12/01, 2000.
- [51] D. Boukerroui, O. Basset, N. Guerin et al., "Multiresolution texture based adaptive clustering algorithm for breast lesion segmentation," *EJU*, vol. 8, no. 2, pp. 135-144, 1998.
- [52] E. A. Ashton, and K. J. Parker, "Multiple resolution Bayesian segmentation of ultrasound images," *Ultrasonic Imaging*, vol. 17, no. 4, pp. 291-304, 1995.
- [53] G. Xiao, M. Brady, J. A. Noble et al., "Segmentation of ultrasound B-mode images with intensity inhomogeneity correction," *IEEE Trans. Med. Imaging*, vol. 21, no. 1, pp. 48-57, 2002.

- [54] G. Pons, J. Martí, R. Martí et al., "Simultaneous lesion segmentation and bias correction in breast ultrasound images," *Pattern Recognition and Image Analysis*, pp. 692-699: Springer, 2011.
- [55] H.-H. Chiang, J.-Z. Cheng, P.-K. Hung et al., "Cell-based graph cut for segmentation of 2D/3D sonographic breast images," in *IEEE ISBI: From Nano to Macro*, 2010, pp. 177-180.
- [56] C.-M. Chen, Y.-H. Chou, C. S. Chen et al., "Cell-competition algorithm: A new segmentation algorithm for multiple objects with irregular boundaries in ultrasound images," *Ultrasound in medicine & biology*, vol. 31, no. 12, pp. 1647-1664, 2005.
- [57] Z. Tu, "Probabilistic boosting-tree: Learning discriminative models for classification, recognition, and clustering," in *IEEE ICCV*, 2005, pp. 1589-1596.
- [58] Z. Hao, Q. Wang, H. Ren et al., "Multiscale superpixel classification for tumor segmentation in breast ultrasound images," in *IEEE ICIP*, 2012, pp. 2817-2820.
- [59] Y. Xu, "A modified spatial fuzzy clustering method based on texture analysis for ultrasound image segmentation," in *IEEE ISIE*, 2009, pp. 746-751.
- [60] K.-S. Chuang, H.-L. Tzeng, S. Chen et al., "Fuzzy c-means clustering with spatial information for image segmentation," *Computerized Medical Imaging and Graphics*, vol. 30, no. 1, pp. 9-15, 2006.
- [61] C. Lo, Y.-W. Shen, C.-S. Huang et al., "Computer-aided multiview tumor detection for automated whole breast ultrasound," *Ultrasonic Imaging*, vol. 36, no. 1, pp. 3-17, 2014.
- [62] B. Liu, H. D. Cheng, J. H. Huang et al., "Fully automatic and segmentation-robust classification of breast tumors based on local texture analysis of ultrasound images," *Pattern Recognit.*, vol. 43, no. 1, pp. 280-298, Jan, 2010.
- [63] P. Viola, and M. J. Jones, "Robust real-time face detection," *IJCV*, vol. 57, no. 2, pp. 137-154, 2004.
- [64] S. F. Huang, Y. C. Chen, and W. K. Moon, "Neural network analysis applied to tumor segmentation on 3D breast ultrasound images," in *ISBI*, pp. 1303-1306, 2008.
- [65] A. A. Othman, and H. R. Tizhoosh, "Segmentation of Breast Ultrasound Images Using Neural Networks," *Engineering Applications of Neural Networks*, pp. 260-269: Springer, 2011.
- [66] F. Milletari, N. Navab, and S.-A. Ahmadi, "V-net: Fully convolutional neural networks for volumetric medical image segmentation," in *IEEE 3D Vision (3DV)*, 2016, pp. 565-571.

- [67] O. Ronneberger, P. Fischer, and T. Brox, "U-net: Convolutional networks for biomedical image segmentation," in MICCAI, 2015, pp. 234-241.
- [68] Y. Xie, Z. Zhang, M. Sapkota et al., "Spatial Clockwork Recurrent Neural Network for Muscle Perimysium Segmentation," in MICCAI, 2016, pp. 185-193.
- [69] W. Zhang, R. Li, H. Deng et al., "Deep convolutional neural networks for multi-modality isointense infant brain image segmentation," *NeuroImage*, vol. 108, pp. 214-224, 2015.
- [70] J.-Z. Cheng, D. Ni, Y.-H. Chou et al., "Computer-Aided diagnosis with deep learning architecture: applications to breast lesions in us images and pulmonary nodules in CT scans," *Scientific reports*, vol. 6, 2016.
- [71] M. H. Yap, "A novel algorithm for initial lesion detection in ultrasound breast images," *Journal of Applied Clinical Medical Physics*, vol. 9, no. 4, 2008.
- [72] J. I. Kwak, S. H. Kim, and N. C. Kim, "RD-based seeded region growing for extraction of breast tumor in an ultrasound volume," *Computational Intelligence and Security*, pp. 799-808: Springer, 2005.
- [73] Y.-L. Huang, and D.-R. Chen, "Watershed segmentation for breast tumor in 2-D sonography," *Ultrasound in medicine & biology*, vol. 30, no. 5, pp. 625-632, May, 2004.
- [74] M. Zhang, L. Zhang, and H.-D. Cheng, "Segmentation of ultrasound breast images based on a neutrosophic method," *Optical Engineering*, vol. 49, no. 11, pp. 117001-117001-12, 2010.
- [75] C. M. Lo, R. T. Chen, Y. C. Chang et al., "Multi-Dimensional Tumor Detection in Automated Whole Breast Ultrasound Using Topographic Watershed," *IEEE TMI*, vol. 33, no. 7, pp. 1503-1511, 2014.
- [76] W. K. Moon, C.-M. Lo, R.-T. Chen et al., "Tumor detection in automated breast ultrasound images using quantitative tissue clustering," *Medical Physics*, vol. 41, no. 4, pp. 042901, 2014.
- [77] P. Jiang, J. Peng, G. Zhang et al., "Learning-based automatic breast tumor detection and segmentation in ultrasound images." in ISBI, 2012, pp. 1587-1590.
- [78] J. Shan, H. D. Cheng, and Y. X. Wang, "Completely Automated Segmentation Approach for Breast Ultrasound Images Using Multiple-Domain Features," *Ultrasound Med. Biol.*, vol. 38, no. 2, pp. 262-275, Feb, 2012.
- [79] J. Shan, H. Cheng, and Y. Wang, "A novel segmentation method for breast ultrasound images based on neutrosophic l-means clustering," *Medical Physics*, vol. 39, no. 9, pp. 5669-5682, 2012.

- [80] B. Liu, H. Cheng, J. Huang et al., "Probability density difference-based active contour for ultrasound image segmentation," *Pattern Recognit.*, vol. 43, no. 6, pp. 2028-2042, 2010.
- [81] C. M. Sehgal, S. P. Weinstein, P. H. Arger et al., "A review of breast ultrasound," *J. Mammary Gland Biol. Neoplasia*, vol. 11, no. 2, pp. 113-123, Apr, 2006.
- [82] D. P. Doane, and L. E. Seward, "Measuring skewness: a forgotten statistic," *Journal of Statistics Education*, vol. 19, no. 2, pp. 1-18, 2011.
- [83] A. T. Stavros, *Breast anatomy: the basis for Understanding Sonography*, in: *Breast ultrasound*, LWW, Philadelphia, 2004, pp. 56-59.
- [84] Y. Z. Cheng, "Mean Shift, Mode Seeking, and Clustering," *IEEE Trans. Pattern Anal. Mach. Intell.*, vol. 17, no. 8, pp. 790-799, Aug, 1995.
- [85] Mean shift: A robust approach toward feature
- [86] M. Xian, Y. Zhang, H. Cheng, F. Xu, B. Zhang, and J. Ding, "Automatic Breast Ultrasound Image Segmentation: A Survey," *arXiv preprint arXiv:1704.01472*, 2017.

## CURRICULUM VITAE

Min Xian  
(2017)

**EDUCATION**

|   |           |
|---|-----------|
| Ph.D. Computer Science  | July 2017 |
| Utah State University (USU)   | GPA: 4.0  |
| Dissertation: “Neuro-Connectedness theory, algorithms and applications” |           |
| Advisor: Heng-Da Cheng  |           |
| M.S., Computer Science  | July 2011 |
| Harbin Institute of Technology (HIT), Harbin, China                     |           |
| B.S., Information Security  | July 2008 |
| Harbin Institute of Technology (HIT), Weihai, China                     |           |

**RESEARCH INTERESTS**

- Robust Data Analysis
- Machine Learning
- Biomedical Data Analysis
- Computer Vision and Image Analysis

**HONORS AND AWARDS**

- Excellent Ph.D. Dissertation Award, Computer Science Department, USU, 2017
- Best Student Paper Award, Computer Science Department, USU, 2016
- Graduate Research and Collaborative Opportunities (GRCO) Grant, USU, 2016
- Travel Grant, International Association of Pattern Recognition Society, 2016
- Travel Grant, USU, March 2016
- Excellent Graduate Student Award, Department of Computer Science, USU, 2015
- Best Presentation Award, Department of Computer Science, USU, 2014
- Golden Prize for Excellent Master, HIT, China, 2011
- Outstanding Master Thesis, HIT, China, 2011
- People Fellowship, Top Grade, HIT, China, 2010

**RESEARCH EXPERIENCE**

**Utah State University, CVPRIP lab, Logan, Utah USA**

Ph.D. Student September 2012 - July 2017

Focus on biomedical data analysis and the build of the theory and algorithms of data topol-



ogy in neutrosophic domain, with the goal to ensure robustness and accuracy on data analysis tasks under weak user interaction and low data quality. Specially, my Ph.D. research includes four parts: (1) Neutro-Connectedness (NC) theory and algorithms; (2) framework for integrating topological properties in image processing; (3) fully automatic breast cancer detection; and (4) left atrium (LA) / left atrial appendage (LAA) thrombus recognition;

(1) Neutro-Connectedness (NC) theory and algorithm

Leading research on NC theory and algorithm for modelling image topology with indeterminacy measurement:

- Building the generalized NC based on region similarity and inhomogeneity, which enable the NC to be independent of top-down prior from the task domain and to have wide potential fields in image processing (image segmentation, saliency estimation, object detection, etc.);
- Designing NC computation algorithm taking polynomial time to output NC values and NC forest simultaneously. The NC forest explores the topological structure of NC and is useful for reducing interaction intensity by providing topological clues.

(2) Framework for integrating topological properties in image processing

Conducted research on the framework of applying NC on image processing tasks:

- Proposed NC-Cut by utilizing pixel-wise appearance information and region-based NC to overcome the user interaction-dependence and high interaction intensity problem in interactive image segmentation. The proposed method was evaluated on two public datasets with 265 images, and outperformed state-of-the-art methods (Grabcut, MILCut, One-Cut and pPBC);
- Applied NC on low quality breast ultrasound (BUS) for breast cancer early detection. The proposed BUS tumor segmentation method can handle the weak boundary problem and can reduce the false positive ratio greatly.

(3) Fully automatic breast cancer detection

Leading research on fully automatic breast cancer detection:

- Tumor segmentation. Designed a segmentation framework for integrating space and frequency domain knowledge, which makes the proposed segmentation method less sensitive to the variation of image brightness and contrast and more robust than the traditional gradient-based methods;
- Tumor detection by modelling attention mechanism. We proposed a novel hybrid saliency estimation framework based on convex optimization for fully automatic BUS tumor segmentation. It models three hypotheses from biological priors and low-level BUS image information;

- Breast cancer detection by using multiple-instance learning (MIL). We modeled breast cancer detection as a MIL problem and proposed the local weighted citation-KNN approach that output the label of each test image by considering local distribution of samples (voters);
- Breast cancer benchmark. To assess current state-of-the-art breast tumor segmentation methods on BUS images, I am working on publishing the first BUS image benchmark in the world. In this task, I collaborate with four radiologists from 3 hospitals to prepare and make publicly available a unique BUS dataset of benign and malignant tumors.

(4) LA/LAA thrombus recognition on transesophageal echocardiography (TEE)  
Designed and implemented a CAD system for LA/LAA thrombus recognition:

- Dynamic texture-based thrombus recognition. Utilized dynamic texture to describe local stiffness by measuring texture difference along TEE sequence; evaluated the CAD on 264 cases (TEE sequences). The experimental results demonstrate that the proposed approach achieve state-of-the-art performance (Sensitivity: 95.6%, Specificity: 95.3%).

## TEACHING EXPERIENCE

**Lab Instructor**, C++ Programming, Harbin Institute of Technology, Spring 2010, 2011  
Lab instructor for undergraduate C++ programming course. Lectured and tutored for the weekly lab session. Developed course projects and graded assignments, exams and projects.

**Teaching Assistant**, Utah State University  
Collaborated on class development, tutored students during office hour or upon requests and graded all assignments and projects for:

- Database Systems(CS5800), Fall 2014, 2016
- Game Development (CS5410, JavaScript and HTML), Spring 2015, 2016
- C++ Programming (CS1400), Fall 2015
- Fuzzy Logic (CS 6630), Spring 2014
- Computer Vision, Pattern Recognition, and Image Processing (CS 5650), Fall 2012

## Mentoring Experience

Mentored graduates' and undergraduates' research projects. Hosted weekly meeting to help students clarify problems, generate new ideas, optimize algorithms, develop experimental schemes, and write research papers. The research projects I have mentored include:

- Deep Learning for pavement crack detection.
- Visual saliency estimation.
- Multiple Instance Learning (MIL) for thrombus detection.

- Breast tumor detection based on visual saliency modelling.
- ECG data analysis. Thesis of undergraduate.

## **WORK EXPERIENCE**

**Research Intern.** March 2009 - August 2009

Pattern Recognition Research Center, HIT, Harbin, Heilongjiang China

- Participated in a project for developing real-time signal processing algorithms running on financial equipment. Designed and implemented an algorithm for fast recognition of the patterns of magnetic signals on banknotes' security thread. This work is very useful for identifying counterfeit banknote (false positive ratio  $\leq 0.005\%$ ), and the algorithm has been embedded in the final product.

## **VOLUNTEER**

- Volunteer for IEEE WACV, Lake Placid, NY March 2016
- Judge for Bridgerland Science and Engineering Fair 2015 & 2016
- Student Support for Faculty Search Committee, Department of CS, USU, 2013
- Served as a volunteer math teacher at Guzhai Elementary School, Summer 2006

## **PROGRAMMING SKILLS**

- Proficient: C++, C, Matlab, R
- Familiar: Java, JavaScript, Python

## **PROFESSIONAL MEMBERSHIP**

IEEE Member and ACM Member

## **PROFESSIONAL SERVICE**

- Reviewed manuscripts for Pattern Recognition, Medical Physics, Neurocomputing, Neural Processing Letters, Journal of Computer Science and Technology(JCST), ICPR, IEEE ICME, and IEEE WACV
- Program Committee member for the International Conference of Pioneering Computer Scientists, Engineers and Educators (ICPCSEE)

## **PUBLICATIONS**

**Articles Submitted for Publication**

- [1] M. Xian, Y. Zhang, H. D. Cheng, F. Xu, J. Ding, "Automatic breast ultrasound image segmentation: a survey," submitted to Pattern Recognition.
- [2] M. Xian, Y. Zhang, H. D. Cheng, F. Xu, K. Huang, "A benchmark for breast ultrasound image segmentation," submitted to IEEE Transactions on Medical Imaging.
- [3] S. Gai, M. Xian, H. D. Cheng, B. Zhang, K. Huang, "Monogenic wavelet modeling using finite mixture of Laplace distribution for image denoising," submitted to IEEE Transactions on Multimedia.
- [4] S. Gai, B. Zhang, M. Xian, K. Huang, H. D. Cheng, "Reduced quaternion matrix based sparse representation and its application to color image processing," submitted to IEEE Transactions on Cybernetics.

### Journal Articles

- [5] M. Xian, Y. Zhang, H.-D. Cheng *et al.*, "Neutro-connectedness cut," IEEE Transactions on Image Processing, vol. 25, no. 10, pp. 4691-4703, 2016.
- [6] M. Xian, Y. Zhang, and H. D. Cheng, "Fully automatic segmentation of breast ultrasound images based on breast characteristics in space and frequency domains," Pattern Recognit., vol. 48, no. 2, pp. 485-497, 2015.
- [7] C. Liu, H.-D. Cheng, Y. Zhang *et al.*, "Robust multiple cue fusion-based high-speed and nonrigid object tracking algorithm for short track speed skating," Journal of Electronic Imaging, vol. 25, no. 1, pp. 013014(1-16), 2016.
- [8] J. Ding, H. Cheng, M. Xian *et al.*, "Local-weighted Citation-kNN algorithm for breast ultrasound image classification," Optik-International Journal for Light and Electron Optics, vol. 126, no. 24, pp. 5188-5193, 2015.

### Conference Articles

- [9] H. Yu, Y. Zhou, H. Qian, M. Xian, *et. cl*, "LooseCut: Interactive Image Segmentation with Loosely Bounded Boxes," IEEE ICIP, 2017 (accepted)
- [10] M. Xian, F. Xu, H. D. Cheng, "EISeg: Effective interactive image segmentation," in ICPR, 2016, pp. 1982 - 1987.
- [11] F. Xu, M. Xian, H. D. Cheng, "Unsupervised saliency estimation based on robust hypotheses," in IEEE WACV, 2016, pp. 1 - 6.
- [12] H. Guan, Y. Zhang, M. Xian, H.D. Cheng, X. Tang, "WENN for individualized cleaning in imbalanced Data," in ICPR, 2016, pp. 456 - 461.

- [13] J. Ding, M. Xian, H. D. Cheng, “An algorithm based on LBPV and MIL for left atrial thrombi detection using transesophageal echocardiography,” in IEEE ICIP, 2015, pp. 4224-4227.
- [14] H. Shao, Y. Zhang, M. Xian, H. D. Cheng, F. Xu, J. Ding, “A saliency model for automated tumor detection in breast ultrasound images,” in IEEE ICIP, 2015, pp. 1424 - 1428.
- [15] M. Xian, Y. Zhang, H. D. Cheng, “A fully automatic breast ultrasound image segmentation approach based on Neutro-Connectedness,” in ICPR, 2014, pp. 2495 - 2500
- [16] H. Yu, M. Xian, X. Qi, “Unsupervised co-segmentation based on co-saliency model and a new global GMM constraint in MRF,” in IEEE ICIP, 2014, pp. 4412 - 4416.
- [17] M. Xian, J. Huang, Y. Zhang, X. Tang, “Multiple-domain knowledge based MRF model for tumor segmentation in breast ultrasound images,” in: IEEE ICIP, 2012, pp. 2021 – 2024

#### **Other Articles**

- [18] H. Shao, Y. Zhang, M. Xian et al., “Breast Ultrasound Image Co-segmentation by Means of Multiple-domain Knowledge,” *Acta Automatica Sinica*, vol. 42, no. 4, pp. 580-592, 2016-04-20, 2016.